

Contents lists available at ScienceDirect

# Materials and Design

journal homepage: www.elsevier.com/locate/matdes





materialstoday

# Simulation of laser impact welding for dissimilar additively manufactured foils considering influence of inhomogeneous microstructure



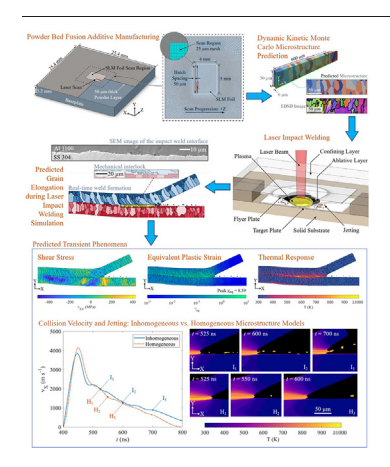
Sumair Sunny <sup>1</sup>, Glenn Gleason <sup>1</sup>, Ritin Mathews, Arif Malik \*

Department of Mechanical Engineering, The University of Texas at Dallas, Richardson, TX 75080, USA

#### HIGHLIGHTS

- Presented is a novel comprehensive modeling framework that captures inhomogeneous microstructure-driven anisotropic effects during simulation of laser impact welding
- The findings reveal grain elongation and alignment resulting from grainboundary sliding, which confirms the development of adiabatic shear banding
- By capturing microstructure, increased plastic strain rates along the weld interface are revealed, resulting in greater plastic heat dissipation
- Unlike existing homogeneous models, findings with the new framework reveal increased jetting with higher temperatures, even at lower collision velocities

### GRAPHICAL ABSTRACT



#### ARTICLE INFO

Article history:
Received 20 October 2020
Received in revised form 13 November 2020
Accepted 29 November 2020
Available online 3 December 2020

Keywords: Impact welding Additive manufacturing Microstructure prediction Finite element numerical modeling

#### ABSTRACT

Introduced is a comprehensive numerical modeling framework that includes microstructure when simulating the laser impact welding (LIW) of metals to study the transient phenomena that occur during weld formation. Such transient phenomena include evolution of shear stresses, plastic strains, thermal response, and material jetting. Inhomogeneous microstructures for two dissimilar foils (aluminum 1100 and stainless steel 304) are first predicted using the Dynamic Kinetic Monte Carlo (KMC) method to simulate laser-based powder bed fusion (PBF-LB) additive manufacturing (AM). These microstructures are subsequently incorporated into an Eulerian finite element (FE) simulation of the LIW process, enabling prediction of grain elongations that result from the varying yield surfaces, stacking fault energies, and grain-boundary sliding effects. Trends in the predicted microstructure deformation patterns show strong agreement with those from experimental images in the literature. Compared to existing homogeneous models, the new framework with inhomogeneous AM microstructure reveals higher collision velocities at the weld interface, resulting in increased plastic strain rates, greater plastic heat dissipation, and increased material jetting with higher jet temperatures. The framework allows for new opportunities to study correlations between grain topography (as well as polycrystalline metal texture) and the transient process phenomena occurring at the impact weld interface.

© 2020 The Author(s). Published by Elsevier Ltd. This is an open access article under the CC BY-NC-ND license (http://creativecommons.org/licenses/by-nc-nd/4.0/).

<sup>\*</sup> Corresponding author. E-mail address: Arif.Malik@utdallas.edu (A. Malik).

<sup>&</sup>lt;sup>1</sup> Joint first author.

#### 1. Introduction

Impact welding involves a rapid collision process, typically lasting a few microseconds, resulting in the formation of a joint that is considered to be primarily mechanical in character [1–3]. A notable benefit of impact welding is the mitigation of undesirable thermomechanical characteristics typically observed in fusion welds between dissimilar metals having large variations in melting temperature. These detrimental characteristics can include formation of brittle intermetallic compounds [2], porosities [4], and micro cracks [5] that occur during the subsequent cooling period.

Experiments conducted as early as the 1960s reveal impact welded joints, as seen in Fig. 1. Abrahamson (1961) (Fig. 1 Top Left) documented observations for an impact weld interface formed when a mild steel bullet (*flyer*) was fired into a copper plate (target) at over 800 m s<sup>-1</sup> with a 30° impact angle [6]. The difference in yield strength together with the relative velocity of the dissimilar colliding materials may explain the elongation in the mild steel grains relative to that seen in the copper target at the weld interface. Cowan et al. (1971) (Fig. 1 Top Right) observed shear elongation of grains along the collision interface for an explosion cladding process wherein a nickel flyer was collided with an AISI 1008 steel target at  $1600 \text{ m s}^{-1}$  [7]. A fluid flow analogy was used to explain formation of the weld interface morphology. Dittrich et al. (2018) (Fig. 1 Bottom Left) used electron backscatter diffraction (EBSD) along with inverse pole figure (IPF) maps to characterize and analyze a Cu-Cu vaporizing foil actuator weld (VFAW) interface and its severe plastic deformation. Their observations revealed the presence of twinning and adiabatic shear bands, as well as static and dynamic recrystallization at the weld interface [8]. Liu et al. (2019) (Fig. 1 Bottom Right) performed VFAW experiments with subsequent peel strength tests for both wrought and PBF-LB additively manufactured 15-5 PH steel specimens. Based on mean impact velocities of 677 m s<sup>-1</sup> and 630 m s<sup>-1</sup> in the wrought and AM flyers, respectively, adiabatic shear bands and cracks were observed near the weld interfaces, in addition to a sheardeformed layer. It was noted that the more elongated grains, observed as the shear-deformed layer became thicker (with increase in impact angle), were indicative of a greater degree of dynamic shear strain [9]. Raoelison et al. studied the interfacial features formed during magnetic pulse welding (MPW) of Al 6060-T6 tubular assemblies. The Al-Al welds were observed to be either straight or wavy in shape. Large shear deformation in grains adjacent to the weld interface caused the grains to evolve from an undeformed equiaxed structure to a flatter elongated morphology, indicating formation of a joint without sliding or debonding [10].

While several impact welding techniques that create solid-state welds of varying scale and geometry have been studied, including explosive, magnetic pulse, vaporizing foil, and gas gun types [2], this work focuses on examination of the transient weld interface behavior during laser induced impact weld formation. Laser impact welding (LIW), shown schematically in Fig. 2, involves a *confined ablation* process [12] wherein a *flyer* is accelerated towards a stationary *target* due to the high-pressure plasma formed during ablation. Collision velocities of several hundred meters per second occur between the flyer and target, which (under the right process conditions) produce a welded joint. Jetting of material from the obliquely colliding metal surfaces is observed, indicating formation of an impact weld [13–16]. Under certain conditions, springback (separation of the flyer from the target foil after impact) is also observed [3,17].

Numerous applications for impact welding are suggested in the literature, ranging from the cost-effective joining of automotive components involving differing materials [2], the joining of AM metal parts sensitive to high heat inputs during fusion welding [9], and lighter beverage can tab end designs, as described in a LIW patent by Daehn and Lippold [18]. Such applications likely require rigorous experimental testing before large scale industrial deployment. To help alleviate the costs and degree of experimental testing, researchers rely on physics-based predictive models of the impact welding process to determine conditions conducive to successful welds. Table 1 provides a comprehensive summary of the state of the art in numerical models developed to date for impact welding processes.

As noted in Table 1, a shortcoming of the existing models is that they neglect the anisotropic effects that modeling microstructural inhomogeneity might have on the transient phenomena predicted during weld formation, or rather, they assume homogeneous grain morphology, with

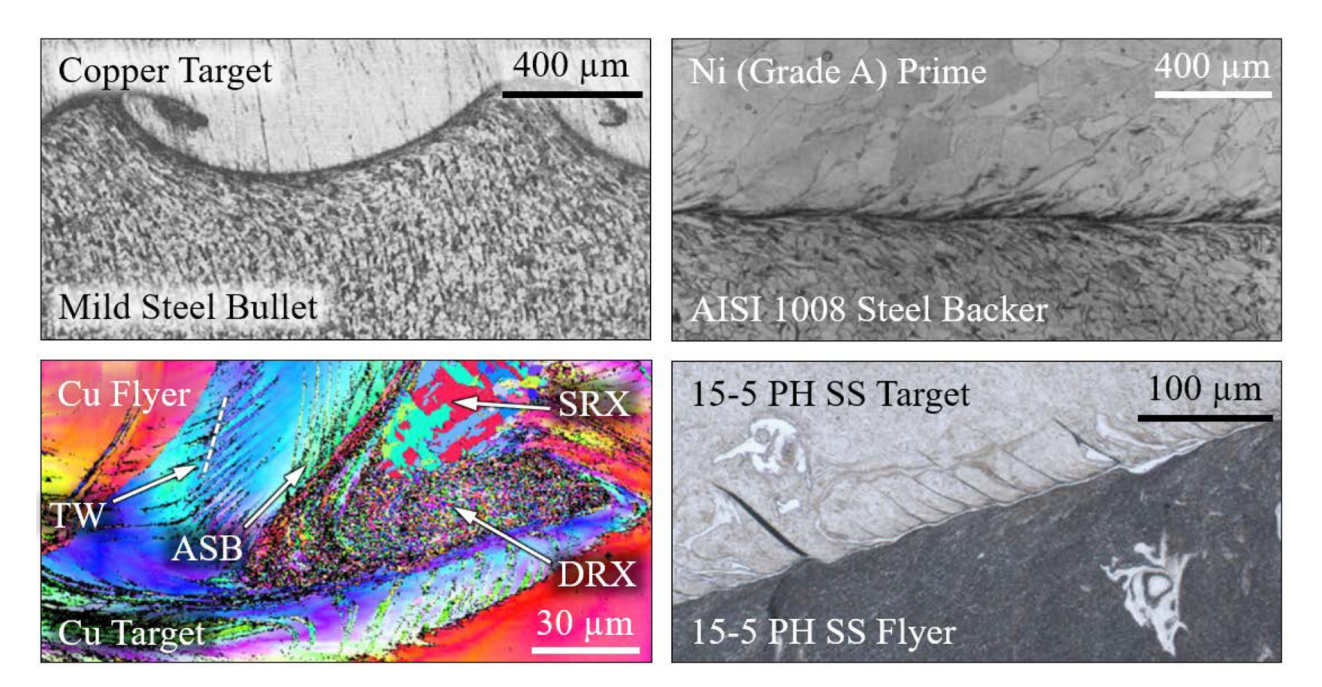


Fig. 1. Images of impact welds documented in literature. (*Top Left*) A mild steel bullet fired into a copper plate, adapted from Abrahamson (1961) [6]. (*Top Right*) Interfacial features of an explosion clad nickel-steel impact weld, adapted from Cowan et al. (1971) [7]. (*Bottom Left*) IPF map of an EBSD image revealing twinning (TW), adiabatic shear banding (ASB), static recrystallization (SRX) and dynamic recrystallization (DRX) from the vortex region of the weld interface formed in a Cu-Cu VFAW experiment, adapted from Dittrich et al. (2018) [8]. (*Bottom Right*) Adiabatic shear banding and microcracks from VFAW experiments on wrought and additively manufactured 15–5 PH steel, adapted from Liu et al. (2019) [9].

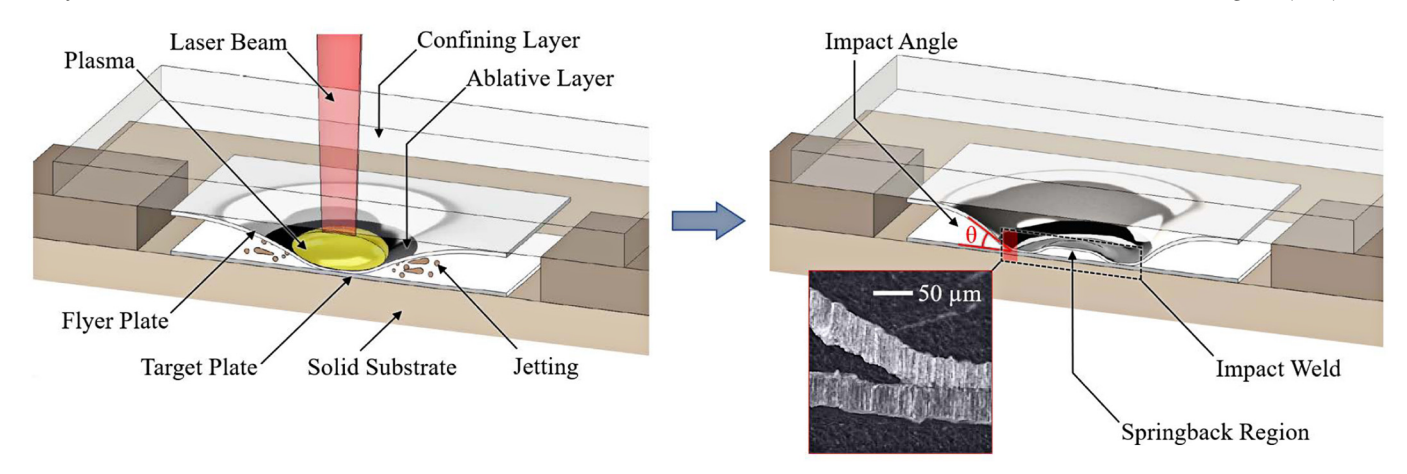


Fig. 2. (*Left*) Schematic of a laser impact welding process featuring necessary components and depicting the expanding plasma that propels the flyer towards the stationary target. Upon impact, material jetting phenomena is observed. (*Right*) The resulting impact weld, also featuring a springback region that develops [3]. (*Inset*) Optical micrograph of a cross section of an Al 1100 – SS 304 laser impact weld, adapted from an earlier publication by the authors [11].

isotropic material definitions for both the flyer and target. This helps garner motivation for the novel framework introduced and demonstrated in this paper. The presented work seeks to illustrate the impact of microstructure modeling when simulating a LIW process featuring inhomogeneous flyer and target foils, as fabricated by selective laser melting (SLM) type additive manufacturing. Accordingly, Section 2 of this paper describes a Lagrangian FE model used to predict corresponding SLM thermal histories of the dissimilar foils. The thermal histories are subsequently exported to the microstructure modeling tool, from which 3D microstructures are predicted and mapped into an Eulerian computational LIW model. Section 3 describes the Eulerian FE formulation used to simulate the LIW process, wherein the model captures both spatial and temporal characterization of the pressure pulse profiles generated via confined laser ablation. Additionally, Section 3 describes the material constitutive models applied to the inhomogeneous foils. A comparison of the transient phenomena predicted for the inhomogeneous model, and a similarly formulated homogeneous model, is presented in Section 4, along with inferences from experimental, analytical, and numerical investigations documented in the literature. Finally, key findings deduced from the inclusion of microstructure in the modeling framework are summarized in Section 5.

# 2. Laser powder bed fusion microstructure prediction and finite element mapping

Microstructure of the flyer and target foils used in LIW studies are influenced by their associated manufacturing method. In this work, the influence of inhomogeneous microstructure, which is typically observed in metal AM [36,37], on the transient, anisotropic thermal and mechanical response during LIW is examined. This section describes the thermal FE powder bed fusion of both Al 1100 and SS 304 specimens, from which the respective time-dependent melt pools (MP) and heat affected zones (HAZ) are determined. The temporally-varying dimensions of the respective foils' MP and HAZ are then used for microstructure prediction using the Dynamic KMC framework [38]. Finally, the predicted microstructures are mapped back to the Eulerian FE model, using material volume fractions (MVFs) for the LIW simulation.

#### 2.1. Laser powder bed fusion finite element model

A single layer, SLM type of PBF-LB transient FE model replicating the thermography experiments described by Heigel et al. [39] at NIST is adopted, as depicted in Fig. 3. Although their experimental work was limited to Inconel 625, the temperature-dependent material models

used herein, for both powder and fused continua, are those for Al 1100 [40] and SS 304 [41]. Further details on the use of SLM to manufacture thin metal foils can be found in [42].

Solid continua in the model include the baseplate and the single powder layer after being melted and cooled below the melting temperature. The powder continua represent a single layer on top of the baseplate prior to melting as a result of the bi-directional laser scans. The thermal conductivity of the powder continua is estimated as 1% that of the solid continua of the same material [43]. Assuming no process parameter associated defects [44], such as lack of fusion (un-melted powder) or porosities (including keyholes), upon reaching melting point the temperature-dependent thermal conductivity curve for powder is transitioned to that of the solid, since the melted region will thereafter be part of the solid (or fused) continua.

Since a Lagrangian FE thermal model is used to simulate the SLM process, linear hexahedral diffusive heat transfer elements are used to discretize the solid and powder continua. These elements only have temperature degrees of freedom active at every node, which reduces the number of calculations at each time increment. Because only a single powder layer is modeled to generate each foil, a discussion on approaches such as *inactive elements* or *quiet elements* [45,46] to account for additional powder layer depositions is omitted. To further reduce the computational expense, as seen in Fig. 3, the scanned region is modeled with 25 µm cubic elements using a structured meshing scheme, while the surrounding powder in the powder bed (not scanned) and the baseplate are discretized using coarser elements of the same type. Solutions for the thermal model, described next, are computed using the implicit solver of Abaqus v6.14.

# 2.1.1. PBF-LB thermal model

The spatially and temporally dependent temperature field for both powder and solid continua in the PBF-LB model is governed by Eq. (1), which gives the 3D heat-energy balance relation [47]. Note that this governing equation has been used for various metal AM models [48–53].

$$\nabla \cdot (k \nabla T) + Q = c_v \rho \frac{\partial T}{\partial t}, \quad \text{for} \quad t \ge 0$$
 (1)

Eq. (1) is applicable ubiquitously within the model for temperature T at time t. Temperature-dependent terms include k,  $c_v$ , and  $\rho$ , which represent the thermal conductivity, specific heat (constant volume) and density, respectively. The dynamic heat energy input Q, arising from SLM laser scans, is discussed in Section 2.1.3. Since only a single layer

 Table 1

 Summary of the state of the art in numerical modeling of impact weld processes.

Author (Year)	Impact Weld Process & Materials	Numerical Model Formulation	Focus of Numerical Investigation	Key Details & Assumptions Relevant to the Present Work
Mousavi et al. (2005) [19]	Explosive welding; Various metals	Eulerian	Velocity     Pressure     Equivalent     plastic strain     Stress (normal     and shear)     Temperature	<ul> <li>Bonding occurs when collision velocity is within a certain threshold range.</li> <li>Impact angles must also be within a critical range for bond formation.</li> <li>Equivalent plastic strain and shear stress values during impact resulted in a wavy interface when beyond a threshold value.</li> <li>Amplitude and wavelength of weld interfaces was dependent on flyer plate thickness.</li> <li>No anisotropy or inhomogeneity mentioned for numerical model.</li> </ul>
Chizari et al. (2009) [20,21]	Gas gun impact welding; Al-Al	Lagrangian	<ul><li>von Mises stress</li><li>Topology of welded joint</li></ul>	<ul> <li>Successful bonding achieved at a 400 MPa shear stress threshold.</li> <li>Impact welding increased roughness of the surface opposite to the weld on the first flyer, affecting quality of subsequent welds on that surface.</li> <li>No anisotropy or inhomogeneity mentioned for numerical model.</li> </ul>
Wang et al. (2012) [22]	Explosive welding; Various metals-Ti	Smoothed Particle Hydro-dynamics (SPH)	Equivalent plastic strain     Pressure     Wavy interface     Shear stress     Jet formation	<ul> <li>Alternating shear stresses noted as key factor for successful bond formation.</li> <li>Greater equivalent plastic strain achieved at higher velocities.</li> <li>Equivalent plastic strain and shear stresses during the process must exceed a minimum (threshold) value to obtain a weld.</li> <li>No anisotropy or inhomogeneity mentioned in material model.</li> </ul>
Wang et al. (2015, 2018, 2019) [17,23,24]	LIW; Al-Al, Al-Cu, Cu-Al, Ti-Cu, Al-SS, SS-Al	SPH	<ul><li>Pressure</li><li>Equivalent plastic strain</li><li>Shear stress</li><li>Velocity</li></ul>	<ul> <li>LIW can lead to both flat and wavy weld interfaces.</li> <li>Springback observed when standoff distance is over a certain threshold.</li> <li>Nanoindentation investigation revealed changes in hardness near interfacial region due to severe plastic deformation and related subsequent effects.</li> <li>No anisotropy or inhomogeneity mentioned for numerical model.</li> </ul>
Nassiri et al. (2016) [25]	VFAW; Al-Al	Arbitrary Lagrangian Eulerian (ALE), SPH	• Shear stress • Temperature • Velocity (collision point)	<ul> <li>Accurate modeling of jetting phenomenon allows for better prediction of experimental design space.</li> <li>Only SPH method showed the jet (and modeled its composition).</li> <li>No anisotropy or inhomogeneity mentioned for numerical models in either formulation.</li> </ul>
Raoelison et al. (2016) [26]	MPW; Al-Al	Eulerian	• Equivalent plastic strain • Temperature	Eulerian models can reproduce jetting kinematics during high strain rate collision by allowing for extreme material deformation.     Shear deformations (elongation/flattening) observed in Al grains near experimental weld interface.     No inhomogeneity mentioned for numerical model.     Materials modeled as isotropic.
Sapanathan et al. (2016) [27]	MPW; Al-Al	ALE, Eulerian	Plastic strain     Temperature     Velocity     (magnitude)	Eulerian simulations can suggest locations of interfacial defects where localized temperature peaks occur.     Orientation of shear strains in Eulerian simulations correspond well to experimental observation.     No inhomogeneity mentioned for numerical models.     Materials modeled as isotropic.
Nassiri et al. (2017) [28]	VFAW; Ti-Cu	ALE, SPH	Equivalent plastic strain     Pressure     Temperature     Velocity (collision point)	<ul> <li>A successful weld was simulated with the predicted peak equivalent plastic strain as high as ~10.</li> <li>Both ALE and SPH methods able to capture simple wavy morphology when found in experiment.</li> <li>Only SPH was able to replicate experimental observations where vorticities occurred.</li> <li>No anisotropy or inhomogeneity mentioned for numerical models in either formulation.</li> </ul>
Lee et al. (2018) [29]	VFAW; Al-Steel	ALE	<ul><li>Temperature</li><li>Velocity</li><li>Weld interface</li></ul>	<ul> <li>Simulation results predicted isolated molten zones, with consequent intermetallic mixing at the weld interface.</li> <li>Flyer thickness and collision angle were both found to correlate with wavelength of weld interface.</li> <li>No anisotropy or inhomogeneity mentioned for numerical model.</li> </ul>
Zhang et al. (2018) [30]	Explosive welding; Al-Steel	SPH	Weld interface     Jetting     Pressure     Temperature	Jet composition dominated by the material (flyer or target) with lowest density.     Key limitations of previous SPH models noted; methods for accuracy improvement implemented.     Improved SPH model shown to be beneficial in studying wave formation mechanisms for impact welds.     No anisotropy or inhomogeneity mentioned for numerical model.
Gupta et al. (2019) [31]	VFAW; Cu-Ti, Al-Steel	Eulerian	Temperature     Velocity     Weld interface	Structural characteristics predicted at weld interface show strong dependence on process parameters (impact velocity, impact angle, material properties).     Impact welds of aluminum to steel rarely show highamplitude wavy patterns (compared to other tested material pairs) per Gupta et al., which is also captured in simulation.     No anisotropy or inhomogeneity mentioned for numerical model.

#### Table 1 (continued)

Author (Year)	Impact Weld Process & Materials	Numerical Model Formulation	Focus of Numerical Investigation	Key Details & Assumptions Relevant to the Present Work
Sadeh et al. (2019) [11]	LIW; AI-SS	ALE, Eulerian	• von Mises stress • Plastic strain • Velocity (magnitude)	Experimentally characterized Gaussian laser pulse energy density.     Experimental laser energy used to model plasma pressure on flyer.     Successfully simulated Al-SS weld formation using plasma load, resulting in more realistic deformed flyer shape and velocity distribution prior to impact.     Specific LIW standoff distances required to achieve successful welds.     Flyer and target modeled as homogeneous and isotropic.
Liu et al. (2019) [32]	VFAW; SS-SS	SPH	Shear strain     Equivalent     plastic strain     von Mises     stress     Temperature	<ul> <li>Adiabatic shear bands experimentally observed.</li> <li>Higher impact angles generate greater shear stress, shear strain, and shear strain rate.</li> <li>Transient high temperatures at weld zones result in interfacial region of very fine equiaxed grains, with greater hardness than the surrounding material.</li> <li>No anisotropy or inhomogeneity mentioned for numerical model.</li> </ul>
Gleason et al. (2020) [33]	LIW; AI-SS	Eulerian	• Equivalent plastic strain • Shear stress • Temperature • Velocity (magnitude)	<ul> <li>Gaussian pressure profile model used per [11]; impact angle found to increase with radial distance from laser spot center.</li> <li>Significant shear stresses predicted in flyer prior to impact, a result of using the more realistic plasma pressure loading condition.</li> <li>Flyer and target modeled as homogeneous and isotropic.</li> </ul>
Lee et al. (2020) [34]	VFAW; Cu-Cu	SPH	• Pressure • Velocity (collision point) • Plastic strain • Temperature	Phenomena difficult to explain using existing numerical methods discussed, including adiabatic shear banding, twinning, and rapid static and dynamic recrystallization. Fig. 1 Bottom Left [8].  No anisotropy or inhomogeneity mentioned for numerical model.  Numerical simulations can provide useful insights into conditions leading to experimentally observed microstructure, even without direct prior modeling of the microstructure.
Cheng et al. (2020) [35]	VFAW; Mg-Steel	Eulerian, Modified embedded-atom method Molecular Dynamics (MD)	Velocity     (collision point     and impact)     von Mises     stress     Equivalent     plastic strain     Temperature	No mechanical interlocking observed in simulated or experimental interfaces at continuum scales between modeled materials in VFAW process.  MD used to model nanoscale diffusion effects due to collision using data from Eulerian simulation output, showing a novel bonding mechanism between Mg and steel.  Single crystal nanostructures established for initial material lattices in MD simulation.

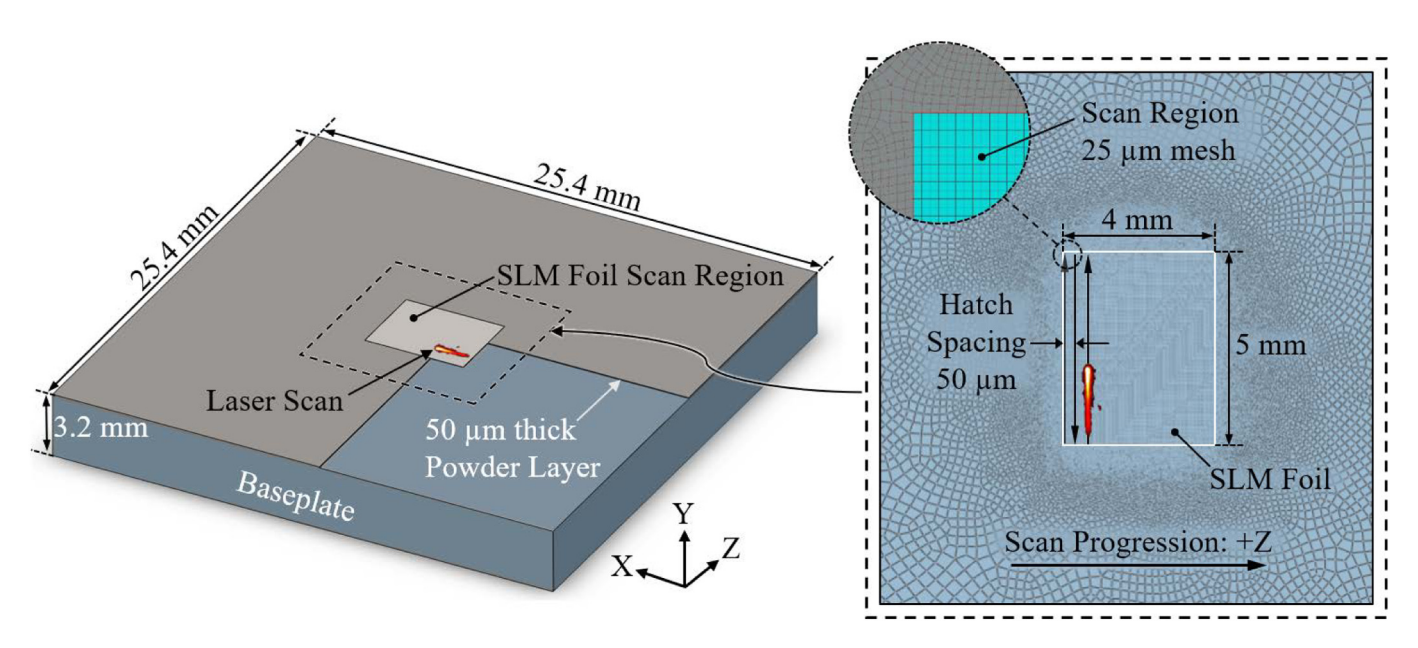


Fig. 3. Schematic of the SLM model to manufacture metal foils (having inhomogeneous microstructure). Dimensions are based on PBF-LB thermography experiments conducted by NIST [39]. Note that a geometrically identical model is used for Al 1100 and SS 304, with only the temperature-dependent material properties, SLM & heat source parameters, and thermal calibration differing.

is modeled, no pre-heating is considered, and thus Eq. (2) enforces ambient (or sink) temperature to the entire model as an initial condition.

$$T(\mathbf{X},0) = T_0 \tag{2}$$

Once the scans commence and heat is added, it is transferred internally and in accordance with the surface energy balance in Eq. (3), which states that conduction from the scanned surfaces to the surrounding powder layer and solid baseplate occurs simultaneously with heat loss via radiation and free convection from the top surface of the build,  $\varphi$ .

$$-k \nabla T \cdot \hat{\boldsymbol{n}} + h(T - T_0) + \psi \varepsilon \left(T^4 - {T_0}^4\right) = 0, \quad \text{on} \quad \varphi \tag{3}$$

In Eq. (3), which is recomputed at every solution time increment,  $\hat{n}$  is a unit surface normal vector, and  $\psi$  is the Stefan-Boltzmann constant (5.6703  $\times$  10<sup>-8</sup> W m<sup>-2</sup> K<sup>-4</sup>). The convective heat transfer coefficient, h, and emissivity,  $\varepsilon$ , are both calibrated parameters in the FE thermal model, and, together with other specific parameters, are adopted from the literature, as detailed next.

#### 2.1.2. PBF-LB process parameters and model calibration constants

SLM process parameters including scan speed v, laser power P, as well as calibration constants such as absorptivity  $\Lambda$ , emissivity  $\varepsilon$ , and convective heat transfer coefficient h, for both materials are adopted from [42,54–56] and are listed in Table 2.

Note that the absorptivity of the respective powders is a function of mean particle size and distribution upon deposition by the recoater blade [57]. Absorptivity is required when computing the dynamic, volumetric heat energy input, discussed next.

#### 2.1.3. PBF-LB heat source model

Since the Dynamic KMC microstructure prediction framework used in this work (discussed in Section 2.2), idealizes the MP and HAZ geometries in the shape of a "single tailed comet", the double ellipsoid Gaussian heat source model of Goldak et al. (1984) [58] is suitable. Eq. (4) describes the volumetric heat source for which the thermal flux distribution is defined as a function of 3D Euclidean space and time.

$$Q = \begin{cases} \frac{6\sqrt{3} \, f_f P \Lambda}{ab c_f \pi \sqrt{\pi}} e^{-3\frac{z^2}{a^2}} \, e^{-3\frac{y^2}{b^2}} \, e^{-3\frac{(x+vt)^2}{c_f^2}}, & x \geq x_i \\ \frac{6\sqrt{3} \, f_r P \Lambda}{ab c_r \pi \sqrt{\pi}} e^{-3\frac{z^2}{a^2}} \, e^{-3\frac{y^2}{b^2}} \, e^{-3\frac{(x+vt)^2}{c_f^2}}, & x < x_i \end{cases} \qquad \text{for} \quad t \geq 0 \tag{4}$$

In Eq. (4), P and v are the SLM laser power and scan speed, respectively. In this work, the heat source is scripted within a "DFLUX" user-subroutine that is recomputed at every time increment during the thermal solution, subsequently updating the position of the scanning laser. It can be treated as a piecewise-continuous function, in this case moving linearly along the X direction, with  $x_i$  being the instantaneous X ordinate. As seen in Fig. 4, for all  $x \ge x_i$ , i.e., the "head" of the comet,  $f_f$  determines the frontal heat distribution fraction, whereas for all

**Table 2** SLM process parameters & calibration constants. [42,54–56].

Parameter	Al 1100	SS 304
P (W)	175	200
v (m s <sup>-1</sup> )	0.195	0.8
Scan Pattern	Bi-directional	Bi-directional
Layer thickness (µm)	50	50
Hatch spacing (μm)	50	50
Λ	0.35	0.4
ε	0.32	0.56
$h (W m^{-2} K^{-1})$	10	10

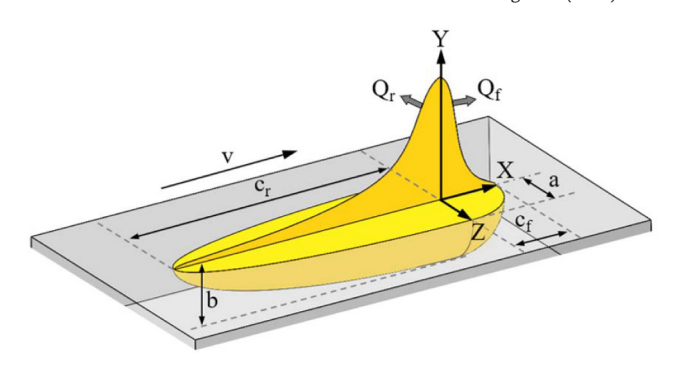


Fig. 4. Double ellipsoid Gaussian heat source model.

 $x < x_{\rm i},$  i.e., the "tail" of the comet,  $f_{\rm r}$  determines the aft heat distribution fraction.

Model calibration leading up to the grain structure prediction is performed in two stages. The first calibration involves replicating thermal histories documented in the literature for studies employing identical process parameters; this is achieved by correcting the input heat flux through adjustment of the double ellipsoid heat source parameters (a, b, c<sub>f</sub>, c<sub>r</sub>). The second calibration is performed by comparison of the simulated microstructure to electron backscatter diffraction (EBSD) images (ref. Fig. 5 Right) that are documented in the same literature [42]. Based on this comparison, the convective heat transfer coefficient may require careful adjustment to modify the degree of intralayer heat accumulation in the PBF model, since it directly influences grain size. While calibrated dimensions for the double ellipsoid geometric parameters are listed in Table 3, it should be emphasized that the ultimate aim of this work is to study the transient anisotropic thermomechanical response when including inhomogeneous microstructure for the additively manufactured foils during LIW, rather than a rigorous and accurate prediction of the specific microstructures.

#### 2.2. PBF-LB microstructure prediction and finite element mapping

While a variety of microstructure prediction methods may be applied, including Cellular Automata (CA) [59,60], Phase Field Modeling (PFM) [61,62], and Kinetic Monte Carlo (KMC) [63–65], in the presented work the Dynamic KMC approach [38] is used. While this work does not intend to compare these different methods, it is worth mentioning that unlike the KMC approach, which is limited to a steady-state MP and HAZ, the Dynamic KMC method can take into consideration temporal variation in the dimensions of the MP and HAZ. Thus, effects of intralayer and interlayer heat accumulation, typically observed in PBF and directed energy deposition (DED) processes [66-70], can be captured. Note that well-calibrated thermal simulations (as discussed above) can mitigate the need for in-situ infrared (IR) thermal imaging to identify the MP and HAZ. On the other hand, simulations over large build volumes suffer the consequence of very high computational cost. The Dynamic KMC framework employed can accept as input either simulated MP and HAZ data or the corresponding thermography data.

Referring to Fig. 3, it is seen that the simulated SLM foil samples have dimensions of 5 mm  $\times$  4 mm  $\times$  50  $\mu$ m. Due to the large computational expense of the LIW simulations (Section 3.2.2), the foils for LIW have dimensions of 600  $\mu$ m  $\times$  6  $\mu$ m  $\times$  50  $\mu$ m, and are thus subsets of the respective SLM foils. Thermal history of every node (Fig. 5 Left), for both the Al 1100 and SS 304 foils subsets, are "probed" frame by frame to extract dimensions of the temporally varying MP and HAZ isotherms. Next, the Dynamic KMC grain structure prediction model is executed and individual grains from the resulting microstructure (Fig. 5 Right) are indexed (i) for subsequent unique material property assignments. For details on the Dynamic KMC microstructure prediction framework the reader is referred to [38]. Note, however, that it is limited to face centered

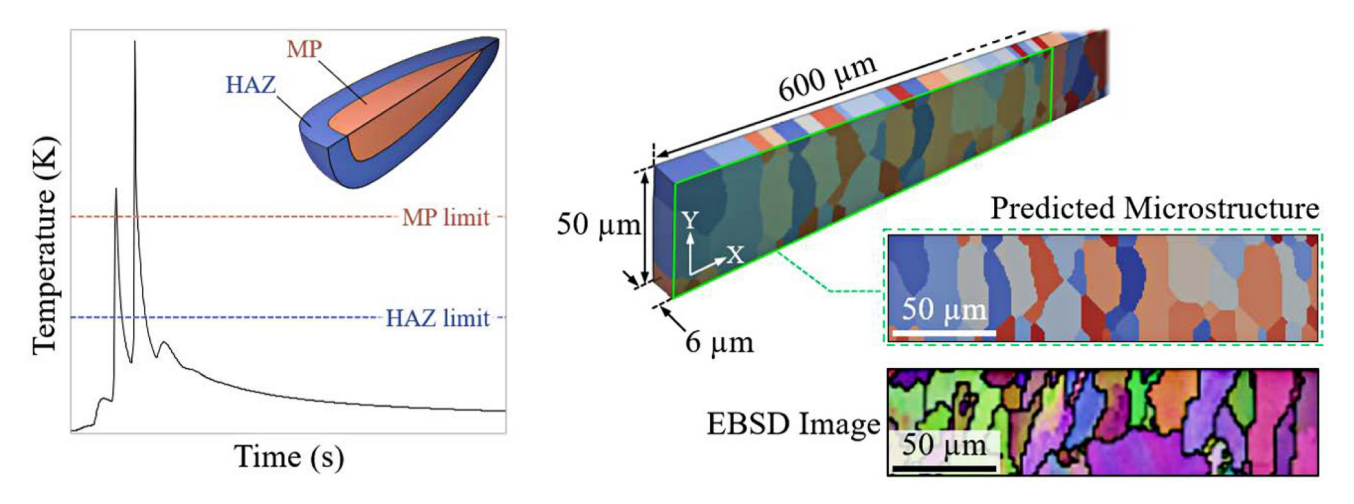


**Fig. 5.** (*Left*) Example of the thermal history of an arbitrary node in the SLM model. A thermal history is extracted for every node and accordingly the dimensions and motion of the MP and HAZ are tracked. This is done for both Al 1100 and SS 304 foils. (*Right*) A comparison of the predicted inhomogeneous microstructure for the SLM SS 304 foil with an EBSD image adapted from [42], where the same material and SLM process parameters were used.

**Table 3**Calibrated heat source model geometric parameters.

Parameter	Al 1100	SS 304
a (µm)	160	180
b (μm)	160	180
$c_f(\mu m)$	276	180
$c_r (\mu m)$	1520	540
$f_f$	1.4	1.4
$f_r$	0.6	0.6

cubic (FCC) and body centered cubic (BCC) crystal structures [71]. Since both A1 1100 and SS 304 exhibit FCC crystal structure [72,73], use of the Dynamic KMC is appropriate. In lieu of such a 3D microstructure prediction tool, 2D EBSD images could also be used, but with assumptions on the out-of-plane grain dimensions.

Once the microstructure is predicted, a Python script is used to spherically fit each volumetric grain  $G_i$  and determine the major diameter  $D_i$ . A material definition  $\mathrm{MAT}(D_i)$  is then generated based on grain-boundary strengthening. Details on the process-dependent material constitutive modeling are discussed in Section 3.4 after a description of the LIW model that follows. The spatial position and volume of individual grains  $G_i$  within a 3D Eulerian FE mesh,  $\xi$ , is used to determine their respective volume fractions. A material volume fraction  $\mathrm{MVF}_i$  represents the volume fraction of  $G_i$  within the Eulerian grid, and has predefined material definition  $\mathrm{MAT}(D_i)$  assigned to it, analogous to a representative volume element (RVE) in a Lagrangian mesh.

### 3. Laser impact welding model

The LIW numerical model discussed in this Section was created to replicate the setup of LIW experiments performed and documented by the authors in earlier work [11]. While the prior research focused on developing, calibrating, and validating predictive models when simulating LIW between Al 1100 and SS 304 foils, the models neglected thermal effects and grain structures, thereby assuming homogeneity and isotropic behavior. The modeling approach here applies similar loading conditions (from the laser induced plasma expansion), but adds thermodynamic degrees of freedom in attempt to elucidate new insights on the dynamic, thermomechanical response during LIW while also investigating anisotropic influences of the inhomogeneous microstructures arising from the SLM process. Given the brief duration of a LIW experiment (~1 s), real-time observations of shear stress propagation, plastic strain evolution, and plastic heat dissipation would be

impractical to obtain. Thus, experimentally-calibrated, physics-based models are needed to glean knowledge of underlying mechanisms that transpire during formation of the mechanical bond [1,3]. A brief overview of the emulated LIW experiment setup (documented in [11]) is presented next.

#### 3.1. Overview of the laser impact welding experiment setup to be modeled

The emulated LIW experiment setup is shown in Fig. 6. A Q-switched, ~17 ns pulsed Nd:YAG laser, operating at 1064 nm wavelength (nearinfrared) generates a 3 I pulse (or shot) that is focused down to a 3.2 mm diameter spot, irradiating a ~25 µm thick matte black painted layer atop the surface of the Al 1100 foil (flyer). Upon absorbing the laser energy, the paint (sacrificial ablative layer) is quickly vaporized, forming expanding plasma that is confined by a transparent borosilicate glass overlay. The expanding plasma accelerates the flyer across a standoff distance of ~260 µm, resulting in a collision with the SS 304 foil (target) which is temporarily affixed to a solid substrate using vacuum grease. In effect, a mechanical "interlock" is formed between the two colliding foils [1,3]. Note that the sacrificial layer prevents melting of the flyer foil, which is affixed to the overlay using transparent doublesided tape. Given the axisymmetric nature of the welded spot [74], symmetry and plane strain boundary conditions are exploited to limit computational expense in the numerical modeling, discussed next.

#### 3.2. An Eulerian model for laser impact welding

Several numerical formulations to model the LIW process can be found in the literature. Some of the more popular approaches involve smoothed particle hydrodynamics (SPH), arbitrary Lagrangian-Eulerian (ALE), Lagrangian, or Eulerian techniques. A comparison of the benefits and challenges of these methods are summarized in Table 4.

While both SPH and Eulerian methods are not prone to excessive distortion-related errors, and can predict material jetting phenomena (discussed in Section 4.5), a trade-off exists considering their respective challenges. An Eulerian model requires very fine mesh, typically with element length,  $L_e$ , lower than 10  $\mu$ m for sufficient accuracy. Considering microstructure MVFs, the  $L_e$  may need to be reduced even further to ensure multiple Eulerian grid elements span the minor diameter of any reconstructed grain to avoid an abrupt simulation crash. On the other hand, an SPH model cannot readily accommodate the Gaussian plasma pressure loading condition (discussed later in Section 3.3), nor is grain boundary tracking very practical. Consequently, an Eulerian approach is adopted in this work, as has been documented in other models

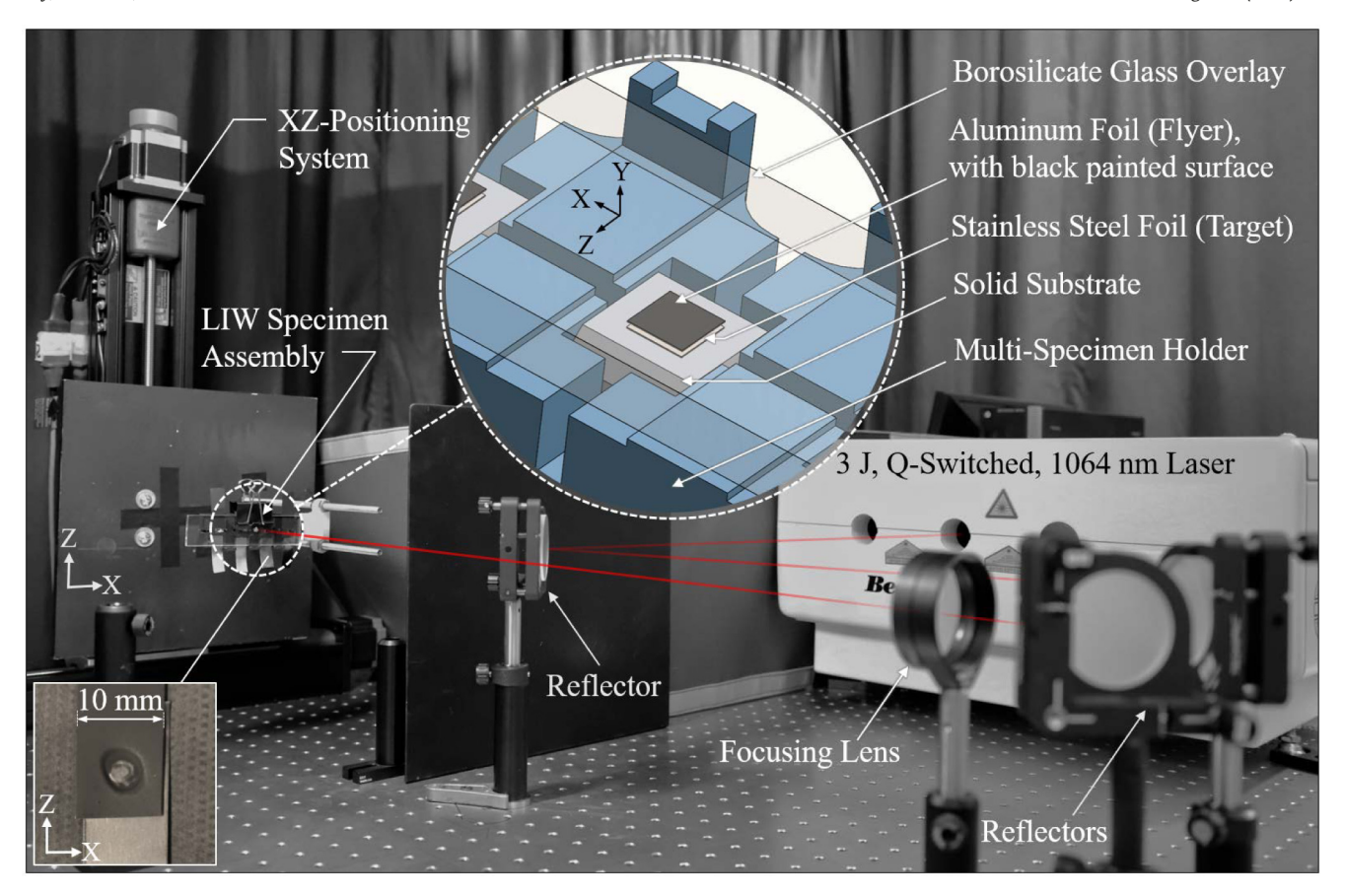


Fig. 6. A photograph of the emulated LIW experiment setup. (Inset, Center) A schematic of the LIW specimen assembly. (Inset, Bottom Left) A photograph of a LIW Al 1100 – SS 304 specimen.

**Table 4**A comparison of numerical formulations commonly used for LIW simulations, adapted from [33].

Numerical Formulation	Benefits	Challenges
Smoothed Particle Hydrodynamics (SPH) [17,22–25,28,30,32,34]	Meshless, discretized particles do not lose accuracy due to distortion or tangling.     Allows for material jetting.	Difficult to apply Gaussian plasma pressure load condition.     Difficult to track exact location of grain boundaries.
Arbitrary Lagrangian-Eulerian (ALE) [11,25,27–29]	Accurate material surface tracking.     Remeshing algorithm maintains mesh quality under certain conditions.	• Shear strain effects in LIW process can still cause mesh distortion at certain collision velocities (>400 m s <sup>-1</sup> ). • Does not allow for material jetting.
Lagrangian [20,21]	Accurate material surface tracking.	<ul> <li>Excessive mesh distortion at colliding interface.</li> <li>Does not allow for material jetting.</li> </ul>
Eulerian <sup>†</sup> [11,19,26,27,31,33] <sup>†</sup> featured in this work	Fixed mesh elements are not susceptible to excessive distortion.     Multiple material assignments allowed in each element to track extreme deformations in collision welds.     Allows for material jetting.	• Accurate material surface tracking requires a fine mesh ( $L_{\rm e} < 10  \mu {\rm m}$ ).

involving extreme plastic deformation [28] and high strain-rate impact welding [26].

## 3.2.1. Governing equations for an Eulerian formulation

The Eulerian formulation is frequently applied to fluid and fluid-structure interaction problems [75] that require extreme strains and strain rates to be modeled, such as those observed in impact welding processes [34]. The Eulerian model is governed by conservation of mass, momentum, and energy as described by Eqs. (5) to (7), respectively.

$$\frac{\partial \rho}{\partial t} + \mathbf{u} \cdot \nabla \rho = -\rho \nabla \cdot \mathbf{u} \tag{5}$$

$$\frac{\partial u}{\partial t} + u \cdot \nabla u = \frac{1}{\rho} (\nabla \cdot \sigma + F_{v})$$
 (6)

$$\frac{\partial E}{\partial t} + \boldsymbol{u} \cdot \boldsymbol{\nabla} E = \boldsymbol{\sigma} : \boldsymbol{\varepsilon}_{\boldsymbol{p}} \tag{7}$$

In these governing equations,  $\boldsymbol{u}$  is a velocity vector in the Eulerian frame,  $\boldsymbol{\sigma}$  is the 3D stress tensor,  $\boldsymbol{F_v}$  is a body force vector,  $\boldsymbol{\varepsilon_p}$  is the plastic strain-rate tensor, and  $\boldsymbol{E}$  is the internal energy per unit mass. Equation (7) considers dissipative heating effects of the plastic deformation, found to be significant near the transient weld front during the LIW process. Equations (5) to (7) are applied ubiquitously over a static grid that discretizes the FE domain for the simulated process.

#### 3.2.2. Laser impact welding Eulerian finite element model

The LIW FE model demonstrated in this work, illustrated in Fig. 7, considers a 90% fraction for the plastic heat dissipation ( $\sigma$  :  $\varepsilon_p$ ) along the impact weld interface [76] by means of a two-way coupling between thermal and mechanical solutions. Accordingly, a linear hexahedral coupled temperature-displacement Eulerian mesh featuring reduced integration is used in the FE model. The grid can be visualized as a lattice of discrete cubic elements having edge lengths,  $L_e$ , of 2 µm. Solutions are computed using the explicit solver of Abagus v6.14. Whilst the model also includes two Lagrangian discrete rigid bodies to represent the transparent borosilicate glass overlay and rigid (or solid) substrate interfaces, these entities do not encompass the weld zone formed between the two dissimilar foils during the simulation, which occurs within the purely Eulerian domain. Within the Eulerian grid, both the 50 µm thick foils, i.e., the aluminum flyer and the stainless steel target, are represented by active MVFs, which are initially positioned adjacent to the upper and lower rigid bodies, respectively. A standoff distance of 260 µm has been experimentally determined to give a successful spot weld and is therefore used in the demonstrated model as an initial spacing between the two foils. As a modeling simplification, the volume fraction of the Eulerian grid that excludes the two foils does not contain any material definition, and is thus treated as a void. Note that experiments on which this work is based featured 10 mm  $\times$  10 mm  $\times$  50 μm foils [11]. Wang et al. [17,23,24], however, documented that transient phenomena (as examined herein) are predicted across the entire weld front, i.e., radially outward from the laser shot center. Accordingly, to reduce computational expense, the radial length (X direction) of the foils considered in this LIW model is limited to  $600 \mu m$ . The out-of-plane thickness (Z direction) is  $6 \mu m$ .

A displacement boundary condition ( $U_z=0$ ) restricting motion along the Z direction is imposed throughout, enforcing a plane strain condition; thus, all the simulated results discussed later in Section 4 only require examination in the XY plane. Rigid body components in the model (see Fig. 7) are constrained in translation ( $U_x=U_y=U_z=0$ ) to emulate the experiment conditions. As noted earlier, a symmetry condition ( $U_x=\theta_y=\theta_z=0$ ) is applied on plane X=0 to further reduce computational cost.

Based on observations from Raoelison et al. (2015) [10], who noted the impact weld joint is formed without sliding or debonding, a no-slip, isotropic Coulomb friction condition defines shear interaction between the colliding metal surfaces. The corresponding coefficient of dry friction,  $\mu$ , is estimated to be 0.6 [77].

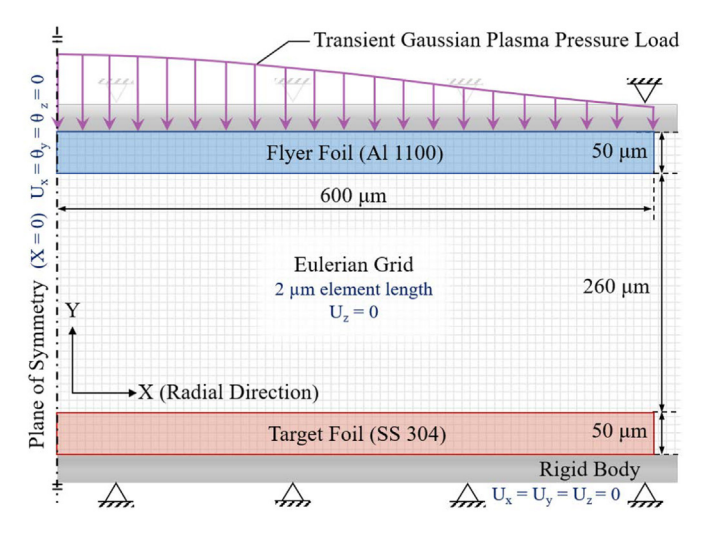


Fig. 7. A schematic of the laser impact welding numerical model applied in this work.

#### 3.3. Laser-induced plasma pressure characterization and modeling

As illustrated in Fig. 7, a plasma pressure field that results from the confined ablation [12] is used to model the load induced by the laser pulse. The associated plasma pressure pulse is considered directly proportional to the square root of laser fluence [78]. Characterization of the laser pulse used in the LIW experiments [11] (and incorporated here) is documented by Hatamleh et al. [79]. In brief, a fast photodetector was used to convert incident optical pulses from the infrared laser to voltage waves, which were then measured using a digital storage oscilloscope to provide the temporal profile. Concurrently, the spatial profile of the incident optical pulses was mapped to a high-resolution 3D point cloud using a beam profiling camera. Equipment specifications can be referenced from [79].

#### 3.3.1. Temporal plasma pressure model

Modeling of the plasma pressure temporal distribution, as well as the peak pressure that results from the ~17 ns full-width, half-maximum (FWHM) transient laser pulse, is based on estimation using the well-established 1D hydrodynamic model developed by Fabbro et al. [12]. Parameters of the hydrodynamic model to be used for the LIW simulation are listed in Table 5.

Fabbro et al.'s model gives a piecewise-continuous, plasma pressure temporal profile, P(t), seen in Eq. (8). The two relationships for pressure at the confined ablation interface represent, respectively, a heating phase  $(t < t_p)$ , and an adiabatic cooling phase  $(t \ge t_p)$  after the laser pulse ceases.

$$P(t) = \begin{cases} \frac{1}{10} \left\{ \left[ \frac{\alpha Z I_0}{2\alpha + 3} \right] \left[ 1 - \left( \frac{L(0)}{L(t)} \right)^2 \right] \right\}^{\frac{1}{2}}, & \text{for } t < t_p \\ P(t_p) \left[ \frac{L(t_p)}{L(t)} \right]^{\lambda}, & \text{for } t \ge t_p \end{cases}$$
(8)

In Eq. (8), the initial plasma thickness, L(0), is estimated to be 10  $\mu$ m. The combined shock impedance (Z) of the two materials at the confined ablation interface, specifically the borosilicate glass ( $Z_g$ ) and the aluminum flyer foil ( $Z_{Al}$ ), is calculated by Eq. (9):

$$Z = \frac{Z_{Al}Z_g}{2(Z_{Al} + Z_g)} \tag{9}$$

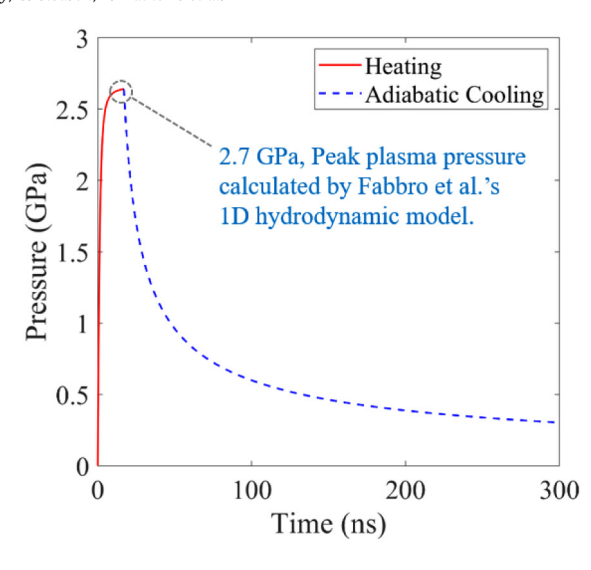
At time  $t_p$  during the LIW simulation, a peak pressure of 2.7 GPa is calculated and used to scale the normalized spatial pressure profile obtained from the 3D point cloud data, as discussed next. The corresponding temporal pressure profile is seen in Fig. 8 *Left*.

#### 3.3.2. Spatial plasma pressure model

Acquired 3D point cloud data for the laser pulse spatial intensity profile is remapped from pixels to radial distance from the spot center, and undulating measurement noise is filtered. To capture the axisymmetric nature of welded spots observed experimentally [74], an axisymmetric bi-variate Gaussian spatial profile, described by Eq. (10), is fit to the data. This simplification facilitates easier incorporation of load to the

**Table 5**Parameters for the 1D hydrodynamic model used to estimate the peak pressure and temporal plasma pressure profile applied in this work, [12,79,80].

Hydrodynamic Model Parameter	Value
FWHM pulse width, $t_p$	~17 ns
Averaged laser pulse flux, $I_0$	$1.8 \; \text{GW cm}^{-2}$
Energy ratio, $\alpha$	0.25
Adiabatic constant, λ	1.4
Glass shock impedance, Z <sub>g</sub>	$1.14 \times 10^6 \mathrm{g}\mathrm{cm}^{-2}\mathrm{s}^{-1}$
Al shock impedance, $Z_{Al}$	$2.75 \times 10^6 \mathrm{g} \mathrm{cm}^{-2} \mathrm{s}^{-1}$



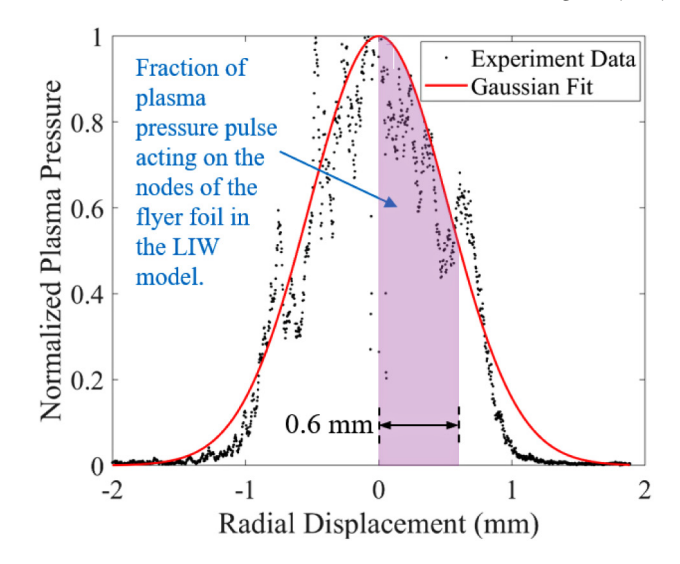


Fig. 8. Experimentally characterized laser pulse plasma pressure (Left) temporal profile, and (Right) spatial profile used to replicate loading conditions in the predictive model.

Eulerian plane strain model, and, more importantly, provides the flyer with a realistic velocity profile and deformed shape prior to impact [11,33]. While the normalized spatial pulse profile is modeled using a Gaussian distribution, note that the magnitude of the pressure load changes according to experimental settings.

$$P(R) = \frac{1}{\sigma_R \sqrt{2\pi}} e^{-\frac{1}{2} \left(\frac{R}{\sigma_R}\right)^2}, \qquad R \ge 0$$
 (10)

In Eq. (10), the normalized pressure *P* is defined as function of radial distance R from the laser spot center, i.e., X = 0 mm. Standard deviation  $\sigma_R$  describes the measured 3D point cloud dispersion from the spot center. The normalized spatial pressure profile is treated as unity at the spot center, and decays radially away (along  $\pm X$  direction in Fig. 8 Right) until it is negligible at  $R=\pm 1.6$  mm (the spot radius). The peak plasma pressure,  $P(t_n)$ , as seen in Fig. 8 Left, obtained from the 1D hydrodynamic model, is used to scale the normalized spatial pressure distribution. Given the small physical dimensions of the simulated LIW domain, only a 600 µm fraction of the laser spatial pressure profile is applied in the LIW model. In the Eulerian LIW grid, the Gaussian plasma pressure profile is enacted by a distribution of concentrated forces divided equally among all the layers of nodes  $n_l$  that span the 50  $\mu$ m thick flyer (Y direction). Equation (11) describes how the distributed pressure P(R) is discretized to concentrated nodal forces  $F_n$  across the radial length R of the laser spot. Considering the cross-sectional area,  $L_e^2$ , of each grid element (in the XZ plane), a peak nodal force magnitude of  $3.24 \times 10^{-4}$  N is calculated to occur during the confined ablationinduced loading phase.

$$F_n(R) = \frac{L_e^2 P(R)}{n_l} \tag{11}$$

## 3.4. Laser impact welding material constitutive model

As discussed earlier, PBF-LB process-parameter specific grains are predicted using the Dynamic KMC microstructure prediction model. While crystal plasticity-finite element (CPFE) methods [81] may be preferable when studying the influence of microstructure, such methods require knowledge of the crystal orientation for individual grains  $G_i$ . Since the Dynamic KMC predictive model does not offer such information, an empirical Hall-Petch (H-P) relation [82,83] is used to determine an equivalent grain-diameter specific

yield strength for the individual grains. Per Eq. (12), grains  $G_i$  are assigned unique yield strengths,  $\sigma_{y,i}$ , based on their respective major diameters,  $D_i$ . This is justified in that the major diameter of non-spherical grains corresponds to the lowest strength direction in a polycrystalline alloy [84]. Although the diameter term in the H-P relation was initially intended to be the averaged grain diameter of a bulk specimen, recent studies discuss the use of individual grain diameters [85].

$$\sigma_{y,i} = \sigma_0 + \frac{k_y}{\sqrt{D_i}} \tag{12}$$

In Eq. (12),  $\sigma_{y,i}$  is the -H-P yield strength for individual grains  $G_i$ ,  $\sigma_0$  is the minimum stress required to initiate dislocation movement (9.7 MPa for Al 1100, 147.4 MPa for SS 304), and  $k_y$  is the strengthening coefficient (41 MPa  $\mu$ m $^{-0.5}$  for Al 1100, 551.67 MPa  $\mu$ m $^{-0.5}$  for SS 304) [86.87]

Considering the extreme plastic deformation that occurs at the high strain rates involved in impact welding [88], along with consequent elevated temperatures due to plastic dissipative heating, the empirically determined yield strengths  $\sigma_{y,i}$  are integrated into a rate and temperature-dependent Johnson-Cook (J-C) model, as given by Eqs. 13 and 14. Thus, a combined J-C H-P approach is used to determine the dynamic flow stress,  $\sigma_{f_i}$  during the LIW simulation. J-C parameters used in the demonstrated LIW model are listed in Table 6.

$$\sigma_{\rm f} = \left[ A + B(\varepsilon_p)^n \right] \left[ 1 + C \ln \left( \frac{\dot{\varepsilon}_p}{\dot{\varepsilon}_0} \right) \right] \left[ 1 - (T^*)^m \right]$$
 (13)

**Table 6**Johnson-Cook parameters. [24].

Parameter	Al 1100	SS 304
A (MPa)	$\sigma_{y,i}$ (ref. Eq. (12))	$\sigma_{y,i}$ (ref. Eq. (12))
B (MPa)	345.5	1500
C	0.001	0.014
$\dot{\varepsilon}_0$ (s <sup>-1</sup> )	1	1
n	0.183	0.36
m	0.895	1
$T_0(K)$	293	293
$T_{m}(K)$	916	1673

**Table 7** Equation of state parameters, [17,90,91].

Parameter	Al 1100	SS 304
$\rho  (\text{kg m}^{-3})$ $c_0  (\text{m s}^{-1})$	2712	7905
$c_0  (\text{m s}^{-1})$	5451.8	4722
S	1.2592	1.441
Γ	2.14	1.93
G (GPa)	27.4	78

$$T^* = \begin{cases} 0, & T < T_0 \\ \left(\frac{T - T_0}{T_m - T_0}\right), & T_0 \le T \le T_m \\ 1, & T > T_m \end{cases} \tag{14} \label{eq:total_total_total_total}$$

Metals, having large bulk moduli and adiabatic index at ambient state, can experience a small increase in entropy as a shock wave propagates through the solid structure [89]. The volumetric stress-strain response in the metal foils, associated to changes in pressure P and volume as a result of the LIW process, can be thermodynamically modeled by the Mie-Grüneisen (M-G) equation of state, given by Egs. 15 and 16. The Hugoniot form employed herein establishes a linear relationship between shock wave velocity  $U_s$  and particle velocity  $U_p$ , where  $c_0$  is the bulk speed of sound within the dissimilar foil materials,  $\eta$  is the ratio of  $U_n$  to  $U_s$ , s is the ratio of change in  $U_s$  to change in  $U_n$ ,  $E_m$  is the internal energy per unit mass, and  $\Gamma$  is the dimensionless Grüneisen parameter describing the thermodynamic material property. Concurrently, the deviatoric stress-strain response of each foil is modeled by Eq. (17), where  $\sigma_d$  is the deviatoric stress, G is the elastic shear modulus, and  $\varepsilon_{el}$  is the deviatoric elastic strain. Equation of state parameters used for the demonstrated LIW model are given in Table 7.

$$P = \frac{\eta \rho c_0^2}{(1 - s\eta)^2} \left( 1 - \frac{\eta \Gamma}{2} \right) + \Gamma \rho E_m \tag{15}$$

$$U_{\rm s} = c_0 + U_{\rm p} \tag{16}$$

$$\sigma_{\rm d} = 2G\varepsilon_{el}$$
 (17)

The aforementioned material definitions are assigned to MVFs in the Eulerian grid using a Python script. As discussed earlier, a small element length  $L_e$  is required to allow a MVF to accommodate multiple Eulerian grid elements across its smallest (or narrowest) dimension. For relatively small grains, e.g., minor diameter  $d_i$  less than 20  $\mu$ m in the model, this can present a problem, since reducing  $L_e$  significantly increases computational expense. Observing that these smaller, sporadically distributed grains are relatively spherical in shape, a single sporadic MVF is modeled to accommodate all of them, with its yield strength assigned via the H-P relation considering their mean major diameter. This is done for both foils.

By modeling each grain as a unique MVF<sub>i</sub>, the respective foils that contain numerous MVFs are considered to have an inhomogeneous microstructure. To offer some perspective on the anisotropic effects from incorporating an inhomogeneous microstructure, another identical LIW simulation is executed considering homogeneous microstructure. In the homogeneous case, only two volume fractions are modeled within the Eulerian grid; one describing the volume of the flyer foil and the other describing that of the target. Each volume fraction is accordingly assigned an isotropic material definition (ref. Tables 6 and 7), wherein the J-C yield strength remains constant throughout the volume of the foils, i.e., 148.4 MPa and 110 MPa, respectively, for the Al 1100 flyer and SS 304 target [24].

The demonstrated modeling approach for LIW of PBF-LB foils, considering their SLM process-driven inhomogeneous microstructures, is summarized in the flowchart of Fig. 9. Results of the LIW simulation, which focus on comparison of the transient LIW phenomena between

the homogeneous and inhomogeneous microstructure cases, are discussed next.

# 4. Results and discussion for the demonstrated laser impact welding predictive model

As stated, this work seeks to build a comprehensive numerical model that can elucidate insights into the transient phenomena that occur during sub-microsecond laser impact welds, and particularly, the effects when incorporating inhomogeneous foil microstructures according to their SLM method of fabrication. For each LIW phenomenon discussed, two cases are presented; one considering the inhomogeneous microstructure and consequential anisotropic behavior for the foils, and the other assuming homogeneity and resultant isotropic behavior for both foils. The transient phenomena predicted and discussed in this Section are compared to experimental observations, as well as to inferences from alternative numerical and analytical approaches documented by other researchers.

#### 4.1. Grain elongation and shear banding

Predictions from a prior study by the authors [33], in which a Gaussian plasma pressure loading condition was applied for a 3.2 mm diameter laser spot, revealed that, as the weld forms, the impact angle (ref. Fig. 2) increases with radial distance away from the spot center (X =0 mm). From experimental observation, Liu et al. [9] determined that more elongated grains would form with an increase in impact angle and the consequent increase in layer thickness. These prior observations relate to results presented in this work; as seen in Fig. 10, at t = 550 ns with the demonstrated model, it is qualitatively evident that grains in the flyer foil have greater elongation radially away from the spot center, i.e., X = 0 mm. This elongation justifies the Eulerian LIW modeling approach over a meshed Lagrangian one. To quantitatively compare the difference in grain elongation among the two foils, Fig. 11 shows the difference in grain aspect ratio, i.e., ratio of major diameter to minor diameter, for both the Al 1100 flyer and SS 304 target, at the initial state (t =0), and after 550 ns have elapsed in the simulation. It is clear from the histograms in Fig. 11 that there is an approximate 2 and 3-fold increase in the predicted grain aspect ratio of the target and flyer, respectively. As per Liu et al. [9], the relatively more elongated grains indicate a greater degree of dynamic shear strain. Liu et al.'s observations also showed evidence of the formation of adiabatic shear bands, as seen earlier in Fig. 1 Bottom Right. Adiabatic shear bands have also been observed by Dittrich et al., (Fig. 1 Bottom Left) [8]. These localized narrow bands are formed at the weld interface due to an adiabatic rise in temperature from plastic heat dissipation, and where thermal softening in the material occurs to a point where it can no longer strain harden, thus inducing plastic flow instability [92-95]. The high shear deformation within these bands can introduce an increase in dislocation density, indicative of work hardening [8,96]. While adiabatic shear bands may be observed in the absence of dynamic recrystallization, the two phenomena have often been found to co-exist [95]. As the fraction of equiaxed grains (having high-angle grain boundaries) within dynamic recrystallization zones near the weld interface increases, there is a corresponding decrease in dislocation density [97], which limits shear strains within the banded regions. A limitation of the presented framework is that it does not model static or dynamic recrystallization phenomena.

Referring again to Fig. 10, at the weld interface the modeled aluminum grains appears to show far greater deformation compared to those in the stainless steel foil. Given the AM process-parameter dependent dimensions of the predicted grains, an obvious difference exists in the range of yield strengths for both foils (depicted by the color map ranges, Fig. 10). The yield strengths for individual grains used in the J-C flow stress material model are predicted via the H-P strengthening method, albeit high strain rates during LIW and extremely different stacking fault energies (SFE) for the respective FCC metals can influence

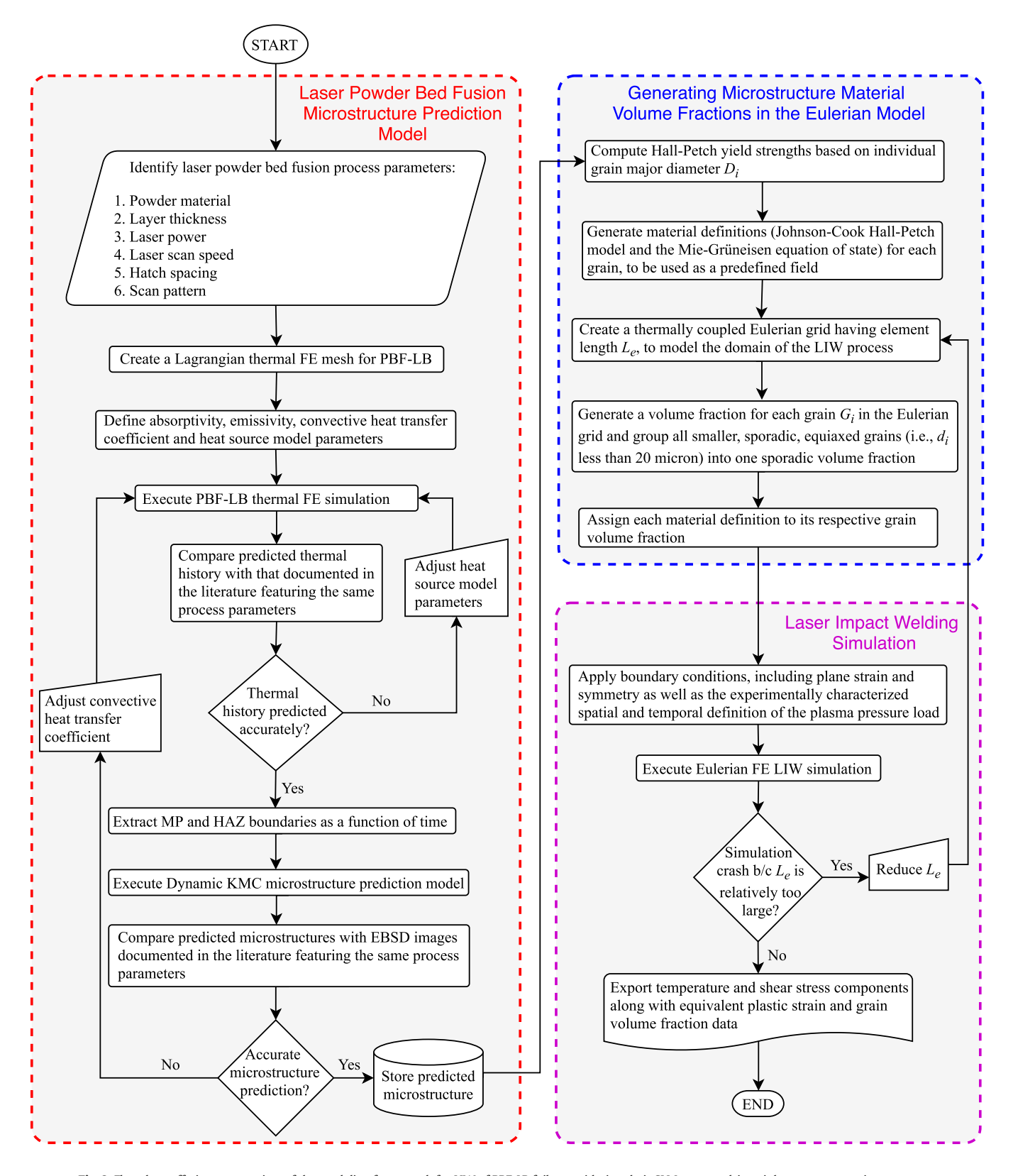
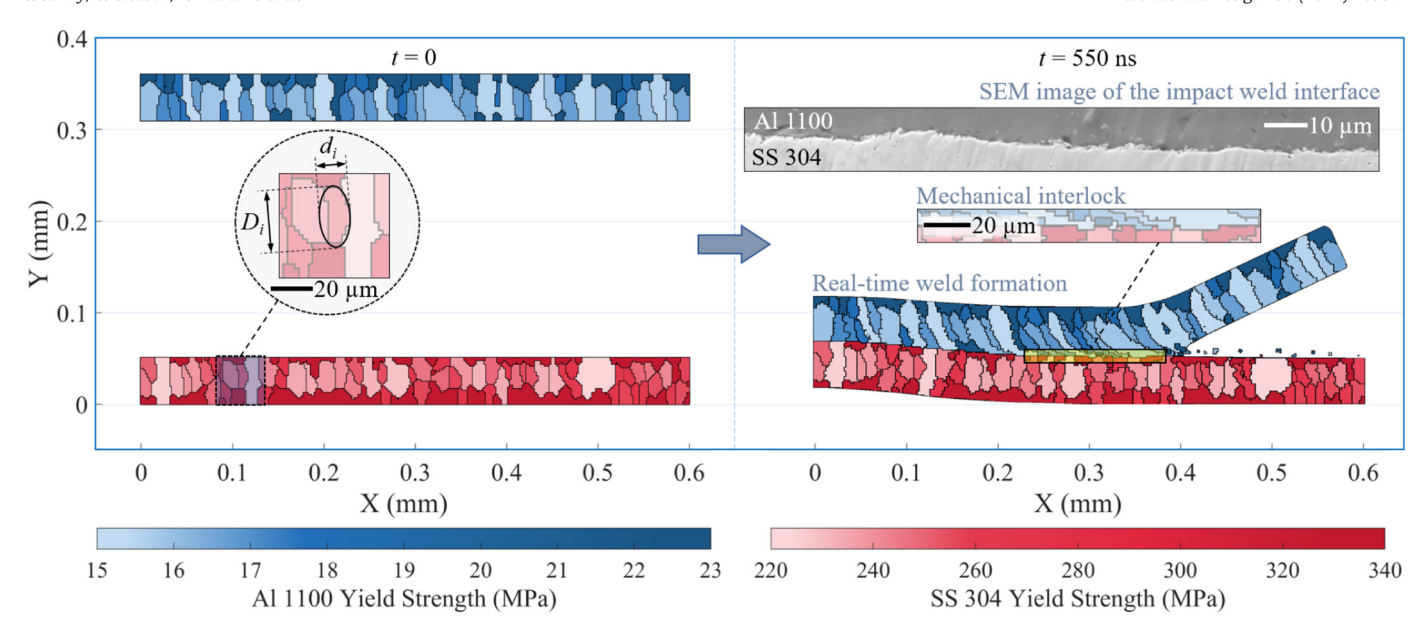


Fig. 9. Flowchart offering an overview of the modeling framework for LIW of PBF-LB foils, considering their SLM process-driven inhomogeneous microstructure.

the choice of H-P coefficients [98]. SFE has a strong influence on critical resolved shear stress needed to initiate cross-slip in FCC metal grains [99]. Aluminum has a high SFE (170 mJ m $^{-2}$ ) and tends to exhibit slip deformation [100]. On the other hand, 304 steel has a relatively low

SFE (~19.2 mJ m $^{-2}$ ) [101], and being a low-carbon steel, at elevated temperatures (~600 K) the strain rate sensitivity increases positively (~0.1), leading to a relatively more homogeneous deformation environment (i.e., reduced heterogeneity in intragranular slip) [102]. These



**Fig. 10.** A qualitative comparison of the grain elongation along the impact weld interface. Note: for the Gaussian load applied, as radial distance increases (+X direction), the impact angle (ref. Fig. 2) also increases. The yield strengths of the respective grains are empirically determined based on H-P strengthening [86,87]. (*Right*) Predicted interlocking at the surface is compared to that observed in an SEM image adapted from an earlier publication by the authors [11], wherein two (non-AM) dissimilar foils were subject to LIW.

differences may explain the predicted variations in aspect ratios between the respective foils in Fig. 11. Note, given the low SFE for steels, the H-P strengthening coefficient will also vary based on alloy composition [98].

Also observed from Fig. 10 *Right*, the grains in the aluminum flyer appear to align such that shear banding can be expected during collision [103]. The predicted shear plane normals in the flyer appear to change direction as impact angle increases, i.e., radially away from the shot center. Interestingly, when looking at Abrahamson's micrographs, wherein a mild steel bullet (*flyer*) was fired into a copper plate (*target*), the grains in the mild steel bullet also appear to elongate in the vicinity of the weld interface [6]. A similar observation can be made from work by Cowan et al. wherein a larger number of grains of AISI 1008 steel appear to align along the interface, as compared to nickel (grade A) [7]. Plausible explanations for the observed grain alignment and elongation can include the impact angle, the relative difference in yield strengths and SFE of the two dissimilar metals, as well as their relative velocities

during the collision. The effect of grain-boundary sliding [104], due to shear movement at the common interface (or boundary) of neighboring grains (within the same material) should also be considered. This form of shear is confined to a small region around the respective grain boundary where the adjacent grains exhibit translation (or sliding) relative to one another. Boundary sliding predicted during the simulation, for a pair of grains in the flyer foil, are depicted in Fig. 12. It can be considered an important mode of deformation at temperatures above 0.45 that of the respective material's melting point. This may explain the microcracks observed by Liu et al. (ref. Fig. 1 Bottom Right).

# 4.2. Influence of microstructure modeling on predicted LIW shear stress distribution

Given the plane strain assumption imposed to reduce computational expense, the predicted shear stress results discussed here are limited to the XY component (i.e.,  $\tau_{XY}$ ). To better understand the transient nature

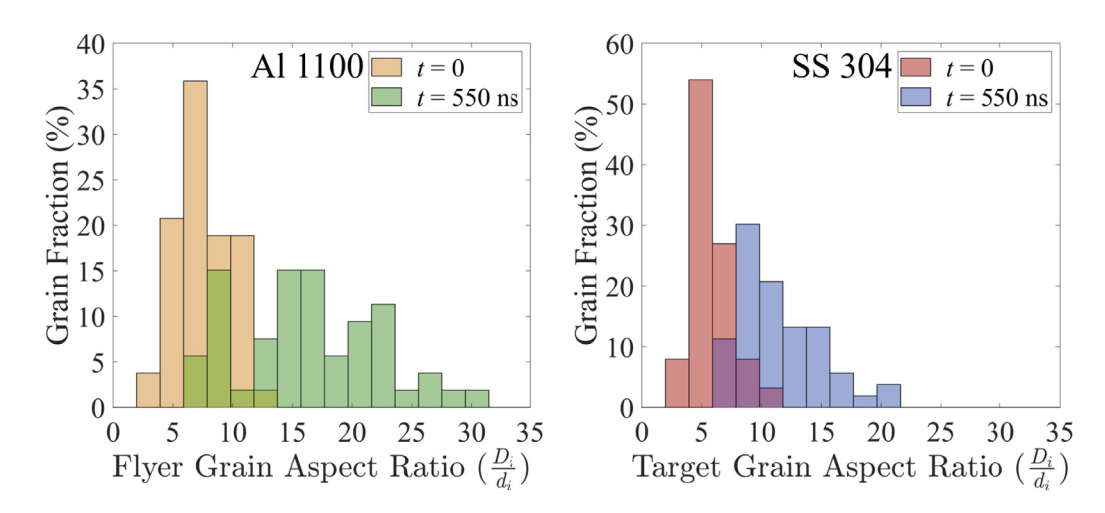
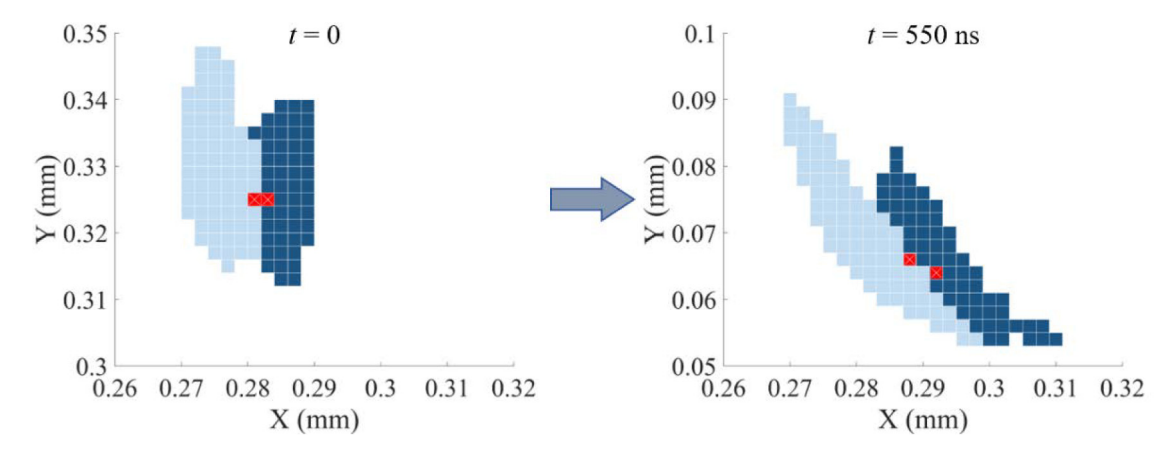


Fig. 11. A quantitative comparison of the ratio of major diameter to minor diameter for grains in the Al 1100 flyer ( $\mathit{Left}$ ) and SS 304 target ( $\mathit{Right}$ ) between the initial state ( $\mathit{t}=0$ ) and after 550 ns in the simulation.

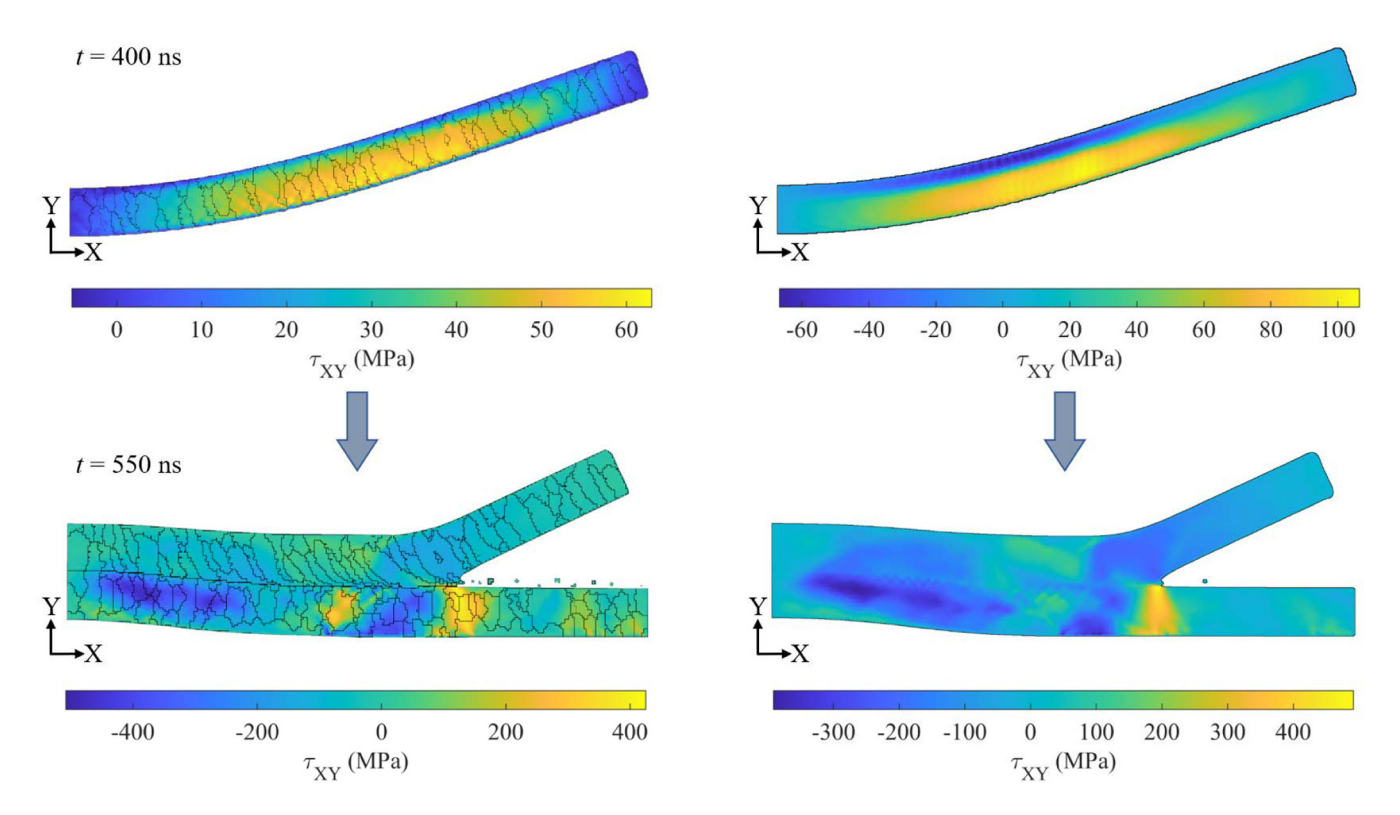


**Fig. 12.** An illustrative example of grain-boundary sliding, predicted by the inhomogeneous model, between two arbitrarily selected neighboring grains in the flyer. (Left) At t = 0, two red boxes, one on each grain, are marked across the shared boundary of the respective grains. (Right) The locations of the same red boxes after 550 ns have elapsed in the simulation, revealing relative sliding motion along the grain boundary. (For interpretation of the references to color in this figure, the reader is referred to the web version of this article.)

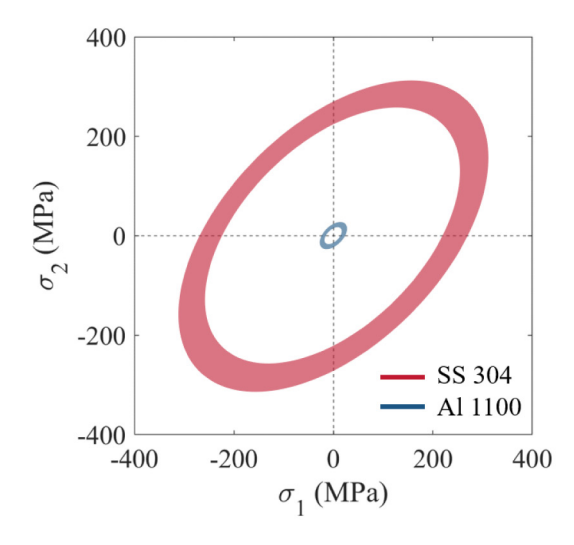
of grain-boundary sliding within the respective foils during the impact weld process, as well as its effect on the distribution of shear stress  $\tau_{\rm XY}$ , Fig. 13 Left shows two frames; one captured just prior to initial contact between the foils (at t=400 ns), and another captured at t=550 ns (during the impact weld formation). Identical frames for the homogeneous case are also featured, ref. Fig. 13 Right, to better assess how microstructure modeling affects  $\tau_{\rm XY}$  distribution during the rapid weld formation. The results reveal a clear difference in  $\tau_{\rm XY}$ , with and without considering microstructure, even before the collision has occurred (t=400 ns). The magnitude of  $\tau_{\rm XY}$  in the homogeneous case ranges from -67 MPa to 107 MPa, whereas that for the inhomogeneous, case shows a relatively smaller range, from approximately -5 MPa to 63 MPa. The reduced shear stress variation seen in the inhomogeneous case may arise due to compensations in the material flow stress

resulting from the varied yield strengths of the grains that stem from H-P strengthening discussed earlier. The bulk of the larger grains in the inhomogeneous microstructure of the additively manufactured foil, having lower yield strengths, will deform with less resistance, thus a reduced range of positive to negative shear stress is predicted.

By t=550 ns, in both the inhomogeneous and homogeneous cases, approximately 0.4 mm (+X direction) of the weld interface has been established. High shear stress magnitudes are predicted to localize in close proximity to the transient weld front in both cases, forming a jet that is characteristic of impact welds [105]. Opposing shear stresses in the flyer and target are suggested to be a feature of successful impact welds [22,106]. In both cases, shear "wakes" trailing the respective weld fronts exhibit an alternating positive-negative pattern, but with a clear difference in their respective ranges. In the inhomogeneous



**Fig. 13.** (*Top*) Shear stress ( $\tau_{XY}$ ) distribution in the flyer prior to initial contact (t = 400 ns) between the two foils. (*Top Left*) inhomogeneous case, and (*Top Right*) homogeneous case. (*Bottom*) Shear stress ( $\tau_{XY}$ ) distribution during impact (t = 550 ns) between the two foils. (*Bottom Left*) inhomogeneous case, and (*Bottom Right*) homogeneous case.



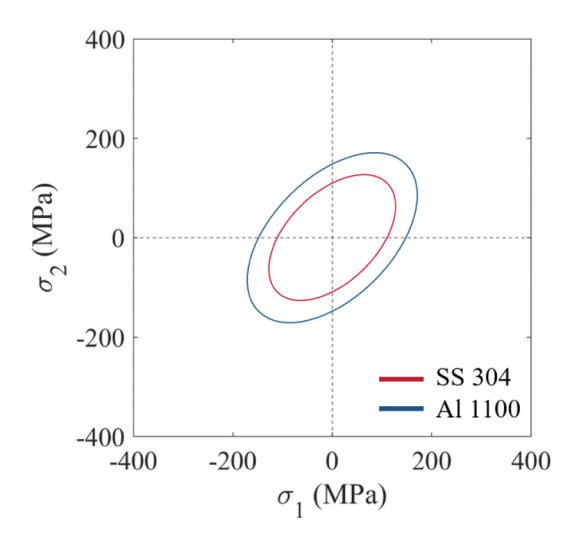


**Fig. 14.** von Mises yield surfaces used in the material definitions. (*Left*) The numerous yield surfaces (bands) for the Al 1100 flyer grains and the SS 304 target grains that stem from introducing H-P strengthening [86,87] into the J-C flow stress material definitions used in the inhomogeneous case. The yield surfaces are calculated based on major diameter, *D<sub>i</sub>*. (*Right*) The yield surfaces for the Al 1100 and SS 304 foils used in the J-C flow stress material definition of the homogeneous case, per [24].

case, the wake varies between extremes of approximately -508 MPa and 425 MPa, whereas in the homogeneous case, the variation ranges from -391 MPa to 492 MPa. There is also a difference in the  $\tau_{\rm XY}$  distribution across the weld interface between the flyer and target; however, the trend predicted when comparing the inhomogeneous case with the homogeneous one is more alike.

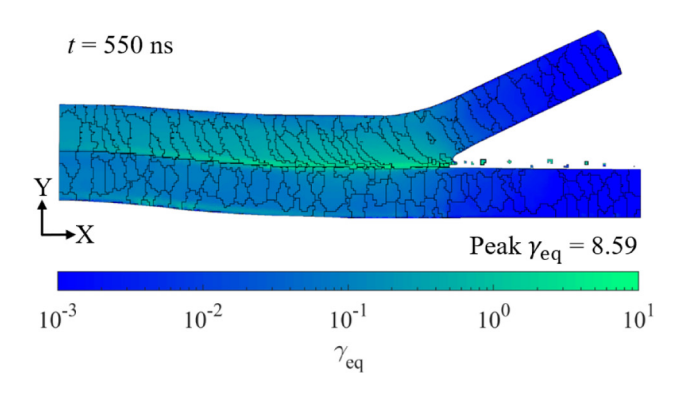
#### 4.3. Yield surface and equivalent plastic strain at the weld interface

To help understand the influence of yield strength on localized grain elongation at the weld interface, equivalent plastic strain,  $\gamma_{eq}$ , is predicted and examined. Note that a monotonic increase in  $\gamma_{eq}$  occurs as the respective material(s) actively yield during the LIW simulation. This will create obvious differences between the inhomogeneous and homogeneous cases given the approach by which the material definitions are applied. For the inhomogeneous case, each grain within a respective foil has a unique yield strength assigned in accordance with H-P strengthening, whereas for the homogeneous case, each foil is assigned a single yield strength. As a result, in the inhomogeneous case there exists a unique von Mises yield surface criterion for each grain, collectively controlling the amount by which the bulk  $\gamma_{eq}$  can increase. In the homogeneous case, each foil has a single (von Mises) yield surface, and  $\gamma_{eq}$  increases whenever the localized state of stress within that foil is on the respective yield surface. The corresponding von Mises yield surfaces for the inhomogeneous and homogeneous cases are illustrated in Fig. 14.

The predicted distributions of equivalent plastic strain,  $\gamma_{eq}$ , for both cases are shown in Fig. 15. Peak values in both cases are predicted to be localized to the weld interface. For the inhomogeneous case, a peak  $\gamma_{eq}$ of 8.59 is predicted at t = 550 ns, whereas in comparison, for the homogeneous case, the peak  $\gamma_{\rm eq}$  (also at  $t=550~{\rm ns}$ ) is 5.93. Similar values of peak  $\gamma_{eq}$  have been predicted by other researchers' numerical models; Lee et al. [34] reported a peak  $\gamma_{eq}$  of 5, localized to the weld interface, when simulating a Cu-Cu VFAW using SPH. Raoelison et al. [26] and Sapanathan et al. [27] simulated an Al-Al MPW via Eulerian and ALE methods and reported peak  $\gamma_{eq}$  of 10 and 6.38, respectively. The predicted microstructure evolution seen in Fig. 15 Left also reveals significant deformation in the Al 1100 flyer near the interface, which is consistent with grain deformation observations from experiments documented by Sapanathan et al. [27] and Raoelison et al. [26]. This is not surprising given the difference in the two dissimilar materials' yield surfaces (Fig. 14 Left). Nonetheless, it should also be noted that the flyer experiences plastic strain prior to impact, which can also induce grain-boundary sliding, particularly given the non-uniform nature of the applied load in the numerical model.

# 4.4. Influence of microstructure modeling on thermal response at the weld interface

In general, material at the weld interface is subject to elevated temperatures resulting from plastic heat dissipation upon collision [76].



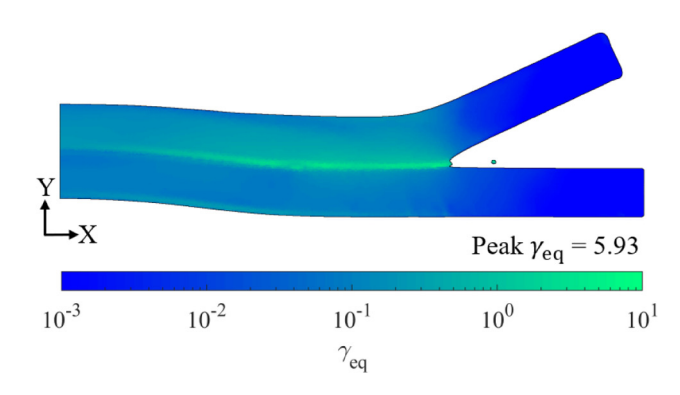


**Fig. 15.** Distribution of equivalent plastic strain,  $\gamma_{eq}$ , at t = 550 ns as predicted by (*Left*) the inhomogeneous case, and (*Right*) the homogeneous case.

These elevated temperatures render the material more conducive to plastic deformation due to thermal softening hence, the rationale for the two-way coupled thermomechanical solution used here, as well as the necessity to capture transient thermal softening effects in the simulation justifies the use of the J-C flow stress model. As seen in Fig. 16, at t = 550 ns, the predicted temperature peaks at the interface (i.e., X = 0.2 to 0.4 mm) trailing the weld front (or collision point) do not exceed 915 K in both cases, hence a reasonable impact weld between the two dissimilar metals can be expected [105]. If the interface temperature predicted were greater than aluminum's melting point, the flyer could melt or even vaporize (if temperature exceeded boiling point) during the LIW process, thus preventing a successful weld [107–109]. Interestingly, while the homogeneous case predicts only two localized peak temperature zones, the inhomogeneous case predicts several highly localized near-peak temperature zones that are distributed along the weld interface. Considering the somewhat similar trend in peaks for the equivalent plastic strain,  $\gamma_{\rm eq}$ , the thermal response in both cases is reasonable; the numerous predicted  $\gamma_{eq}$  peaks in the inhomogeneous case are attributed to a mix of elongated and sporadic equiaxed grains, with varying yield surfaces (per their respective material definitions), that meet during impact along the weld interface with consequent plastic heat dissipation. A similar dispersed thermal response at the interface was predicted by Lee et al.'s SPH model [34]. As mentioned in their work, a shortcoming of existing numerical techniques, however, is their inability to properly model both localized friction and the thin layer of gas compressed as the flyer and target are brought into contact. Such factors will affect the predicted localized thermal response across the collision interface. In addition, EBSD images of the Cu-Cu VFAW interface documented by Dittrich et al. (ref. Fig. 1 Bottom Left) reveal regions of shear banding and deformation twins, as well as static and dynamic recrystallization [8]. They mention that building a numerical model to predict recrystallization resulting from the collision velocity, v<sub>X</sub>, and the rapid time frame within which thermally activated nucleation and growth would have to occur, is very difficult, however.

#### 4.5. Influence of microstructure modeling on collision velocity and jetting

Robinson (1974) mathematically modeled the mechanics of wave formation in impact welding and concluded that when shear strain rates exceed a critical value (10<sup>7</sup> s<sup>-1</sup>), metals exhibit inviscid fluid behavior, with the formation of an inviscid shear layer and an incompressible inviscid jet [88]. Below this critical strain rate, metals behave like a viscid fluid. Robinson (1976) extended his earlier work to study the effects of velocity and viscous energy dissipation on jet formation [109]. He concluded that melting can occur at sufficiently high velocity, subsequently weakening the mechanical bond formed, while at sufficiently low velocities viscous dissipation removes energy necessary for jet formation. Wang et al. concurred with Robinson's inferences; in LIW, upon high speed collision, pressure developed may exceed the yield strength (s) of the material(s) such that solid matter at the weld front demonstrates the characteristics of a low-viscosity liquid [76]. While both the demonstrated cases seen in Fig. 16 exhibit jetting, the inhomogeneous case predicts a relatively greater quantity of jetted material. At t =550 ns, much of the jetted material is below 2600 K, indicating that both aluminum and steel may co-exist in the jetted volume, although a few jetted particles in the both cases are predicted to reach temperatures as high ~2900 K (neglecting effects of radiative and convective cooling). This temperature is just below the boiling point (BP) of SS 304 [108] but surpasses that of Al 1100 (~2700 K) [110], indicating that the aluminum volume fraction might vaporize completely, leaving steel to dominate the jetted volume. This contradicts inferences made by Zhang et al. (2018) [30] who deduced from their SPH model that the lower density material will dominate the jet. Zhang et al.'s inference may only hold true whilst jet temperatures do not exceed the BP of the materials involved. Based on conclusions drawn by Robinson [88,109] and Wang et al. [76], the relationship between the jet and collision velocity v<sub>X</sub> is examined as seen in Fig. 17. Impact initiates after 400 ns have elapsed in the simulation; during the first 400 ns, a plasma pressure load (representing confined ablation) is applied on the flyer, which subsequently accelerates towards the target. Once the collision initiates (t = 400 ns), the collision point appears to accelerate uniformly for the next ~50 ns, followed by an unsteady deceleration in both the inhomogeneous and homogeneous cases. Given the difference in predicted v<sub>X</sub> profiles, by 800 ns a radial weld length (X direction) of ~598 µm has formed in the inhomogeneous case, whereas the homogeneous case exhibits a radial weld length of ~545 µm. Three frames from both curves are probed to visualize the predicted jets, as seen in Fig. 17 (note that given the immense temperature range variation within the

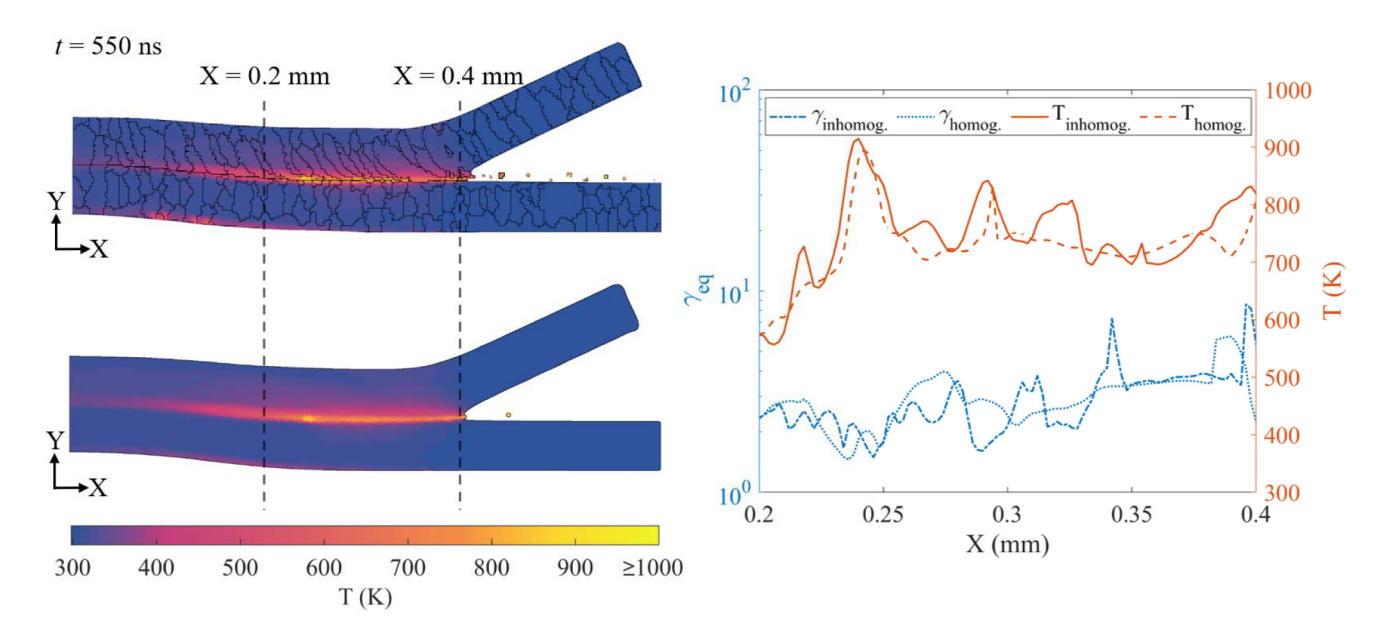


**Fig. 16.** Transient thermal response at t=550 ns, resulting from plastic heat dissipation as predicted by ( $Top \, Left$ ) the inhomogeneous case, and ( $Bottom \, Left$ ) the homogeneous case. While the temperature in the jet exceeds 1000 K, the temperature range displayed in this figure is limited to 1000 K to draw focus to the thermal response at the weld interface. (Right) A comparison of equivalent plastic strain,  $\gamma_{eq}$ , and temperature, T, at the weld interface (i.e., N=0.2 to 0.4 mm) trailing the collision point for the two cases, at t=550 ns.

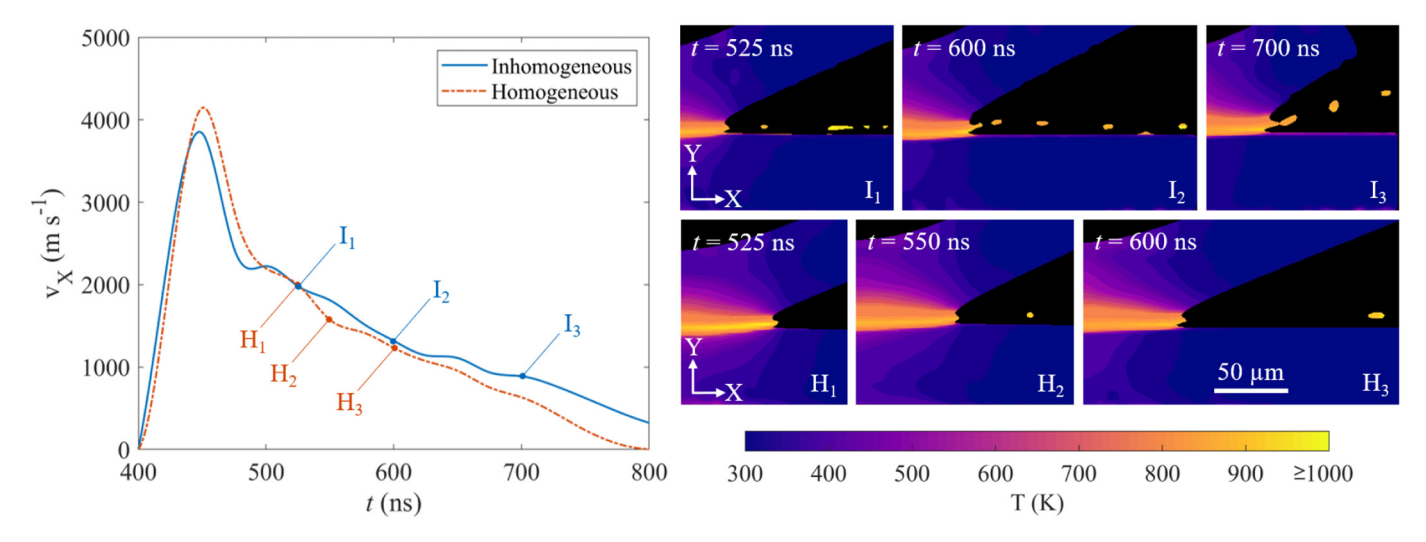


**Fig. 17.** (*Left*) A plot comparing the collision velocity  $v_X$  vs. time t for the inhomogeneous and homogeneous cases. (*Right*) Frames captured from the respective inhomogeneous (I) and homogeneous (H) simulations, illustrating the relative differences in volume of jetted material, as well as weld front temperature, T, predicted for the two cases. Note that grain boundaries are omitted in the inhomogeneous frames (I) to offer more clarity of the dynamic weld front.

jets, all jetted material exceeding 1000 K is grouped into the same isotherm). From the multiple frames captured, the inhomogeneous case exhibits a substantially greater jetted volume compared to the homogeneous one. Considering that both cases apply the same boundary and loading conditions, it can be postulated that the difference in  $v_x$  stems from grain-boundary sliding effects [104] within the respective foils. due to the variations in yield surfaces among individual grains. The predictions, when comparing both cases, agree with Robinson's findings in that a lower v<sub>x</sub> results in reduced jetting, however, it can be argued that during the period of 500 to 600 ns, the velocities do not differ quite as significantly as the jetting phenomenon appears to. Furthermore, referring to Fig. 17 Right, the third inhomogeneous frame (I<sub>3</sub>) shows more jetting compared to any of the three homogeneous frames  $(H_{1-3})$ , despite having a relatively lower v<sub>X</sub>. Bearing this in mind, two insights can be deduced from these predictions: (1) A higher v<sub>X</sub> can result in increased plastic strain rates and consequently greater amounts of plastic heat dissipation at the interface, possibly explaining the differences in the predicted quantity of jetted material as well as the jet temperature; (2) inclusion of microstructure in the LIW numerical model has a significant effect on the predicted jetting phenomenon, beyond its influence on vx. While some degree of correlation may exist between these insights, it would require a comprehensive parametric assessment, which is not within the scope of this work.

# 4.6. Computational expense and efficacy of microstructure inclusion in a LIW numerical model

Finally, to draw comparisons on relative computation times for the inhomogeneous and homogenous cases, the respective FE LIW models were run on two Intel Xeon E5–2670 processing cores (2.3 GHz), equipped with 132 GB of RAM. The homogeneous case was completed in ~6.5 h, while the inhomogeneous case required ~43 h. Note that the inhomogeneous case requires the additional prerequisite prediction of an AM thermal history from which the subsequent microstructure prediction is performed. The AM thermal simulation (for the FE model illustrated in Fig. 3) was run on five Intel Xeon E-2176 M processors (2.7 GHz), equipped with 64 GB of memory. The simulation completed in ~104 h. The microstructure prediction simulation for the smaller subset of the AM foil, was run on eighty Intel Xeon E5-2698V4 processors (3.6 GHz), equipped with 512 GB of RAM. The aluminum foil microstructure simulation completed within ~7.5 h, while that of the steel took ~5 h. The difference in simulation time is attributed to the

nature of temporal variations in size of the MP and HAZ [38]. The overall inhomogeneous case simulation time detailed here does not factor time spent re-calibrating any of the respective models involved, as outlined in Fig. 9. Thus, making a comparison of simulation time between the two cases is somewhat misleading: As demonstrated in this work. when microstructure is considered in the LIW model, predicted transient characteristics that manifest, including shear stress distribution, thermal response at the interface, equivalent plastic strains, and material jetting, appear considerably different to those predicted in a model that assumes material homogeneity. In addition, grainboundary sliding effects, as well as the multiple yield surfaces, introduced through microstructure inclusion in a LIW numerical model, offer new insights towards grain elongation, shear banding, and collision velocity. Capturing such phenomena experimentally in real-time is challenging, and thus efficacy of microstructure inclusion in the physics-based LIW numerical model can be appreciated.

## 5. Conclusion

This paper introduces and demonstrates a novel framework that incorporates a PBF-LB AM inhomogeneous microstructure in a LIW numerical model. While other researchers have built numerical models (ref. Tables 1 and 4) to study transient phenomena during LIW, their predictive models neglect the physical presence of microstructure, thereby assuming homogeneity with isotropic material definitions. A limitation of the isotropic, homogeneous modeling is that grain elongation, observed as early as the 1960s via optical microscopy, is not revealed, nor do its consequent effects manifest. The inclusion of microstructure in the model, with associated anisotropy, reveals the following key findings:

- Given the Gaussian load distribution, as the weld forms, the impact angle increases, and consequently more grain elongation is exhibited, indicative of increased dynamic shear strain. The predicted alignment of elongated grains at the interface suggests the occurrence of shear banding, as has been experimentally observed.
- The alignment of grains as elongation occurs stems from grain-boundary sliding due to shear movements confined to the interface between adjacent grains within the respective foils. The effect is more prominent with elevated temperatures ( $\sim 0.45 T_m$ ) predicted at the weld interface.
- A unique von Mises yield surface is modeled for every grain, resulting in an equivalent plastic strain distribution that may reveal

several localized peaks. This can vary based on the spread and quantity of elongated grains and relatively smaller equiaxed grains in each of the foils that come into contact. The consequent plastic heat dissipation leads to dispersed temperature peaks along the weld interface.

- Grain-boundary sliding within the respective foils, resulting from variations in yield surfaces among individual grains, gives rise to relatively higher collision velocity. A consequent increase in plastic strain rates at the interface, along with greater amounts of plastic heat dissipation, may explain the increased quantity of jetted material as well as greater jet temperatures.
- The demonstrated framework enables the incorporation of PBF-LB AM foils in LIW simulations to directly capture inhomogeneous microstructure driven anisotropy and reveal the consequential effects on transient phenomena occurring at the weld interface, including shear stress distribution, equivalent plastic strain, thermal response, collision velocity, and jetting. The work provides a new tool for researchers to study the effects of various AM process parameters and their associated grain structures on the transient phenomena at the impact weld interface.

#### Data availability

The raw/processed data required to reproduce these findings cannot be shared at this time as the data also forms part of an ongoing study.

#### Credit author statement

All authors contributed to the study conception and design. Model development and analysis were performed by Sumair Sunny, Glenn Gleason and Ritin Mathews. The first draft of the manuscript was coauthored by Sumair Sunny and Glenn Gleason while remaining authors commented on previous versions of the manuscript. All authors read and approved the revised manuscript. Dr. Arif Malik supervised the project and acquired the funding. Dr. Arif Malik also reviewed and edited the presented work.

# **Declaration of Competing Interest**

The authors declare that they have no known competing financial interests or personal relationships that could have appeared to influence the work reported in this paper.

#### Acknowledgment

The authors acknowledge support in part from the U.S. National Science Foundation, grant no. CMMI-1762722. Any opinions, findings, or conclusions expressed in this paper are those of the authors and do not necessarily reflect the views of the U.S. National Science Foundation.

### References

- B. Crossland, A. Bahrani, Fundamentals, of explosive welding, Contemp. Phys. 9 (1968) 71–87.
- [2] W. Cai, G. Daehn, A. Vivek, J. Li, H. Khan, R.S. Mishra, M. Komarasamy, A State-ofthe-Art Review on Solid-State Metal Joining, Journal of Manufacturing Science and Engineering 141, 2019.
- [3] X. Wang, H. Tang, M. Shao, H. Jin, H. Liu, Laser impact welding: investigation on microstructure and mechanical properties of molybdenum-copper welding joint, Int. J. Refract. Met. Hard Mater. 80 (2019) 1–10, https://doi.org/10.1016/j.ijrmhm. 2018.12.016.
- [4] W. Liu, H.-P. Wang, F. Lu, H. Cui, X. Tang, Investigation on effects of process parameters on porosity in dissimilar al alloy lap fillet welds, Int. J. Adv. Manuf. Technol. 81 (2015) 843–849.
- [5] C. Wang, L. Cui, G. Mi, P. Jiang, X. Shao, Y. Rong, The influence of heat input on microstructure and mechanical properties for dissimilar welding of galvanized steel to 6061 aluminum alloy in a zero-gap lap joint configuration, J. Alloys Compd. 726 (2012) 556-566.
- [6] G.R. Abrahamson, Permanent periodic surface deformations due to a traveling jet, J. Appl. Mech. 28 (1961) 519–528.

- [7] G. Cowan, O. Bergmann, A. Holtzman, Mechanism of bond zone wave formation in explosion-clad metals, Metall. Mater. Trans. B 2 (1971) 3145–3155.
- [8] T. Dittrich, The Characterization and Analysis of A Pseudo Single-grained Copper Impact Weld Interface in Regards to the Effects of Severe Plastic Deformation, Ph. D. thesis, The Ohio State University, 2018.
- [9] B.C. Liu, A. Palazotto, A. Vivek, G.S. Daehn, Impact welding of ultra-high-strength stainless steel in wrought vs. additively manufactured forms, Int. J. Adv. Manuf. Technol. 104 (2019) 4593–4604.
- [10] R.N. Raoelison, T. Sapanathan, N. Buiron, M. Rachik, Magnetic pulse welding of al/al and al/cu metal pairs: consequences of the dissimilar combination on the interfacial behavior during the welding process, J. Manuf. Process. 20 (2015) 112–127.
- [11] S. Sadeh, G.H. Gleason, M.I. Hatamleh, S.F. Sunny, H. Yu, A.S. Malik, D. Qian, Simulation and experimental comparison of laser impact welding with a plasma pressure model, Metals 9 (2019) 1196.
- [12] R. Fabbro, J. Fournier, P. Ballard, D. Devaux, J. Virmont, Physical study of laser-produced plasma in confined geometry, J. Appl. Phys. 68 (1990) 775–784.
- [13] G.R. Cowan, A.H. Holtzman, Flow configurations in colliding plates: explosive bonding, J. Appl. Phys. 34 (1963) 928–939.
- [14] A. Shtertser, B. Zlobin, Flows, strains, and the formation of joints in oblique collision of metal plates, J. Appl. Mech. Tech. Phys. 56 (2015) 927–935.
- [15] J. Bellmann, J. Lueg-Althoff, B. Niessen, M. Böhme, E. Schumacher, E. Beyer, C. Leyens, A.E. Tekkaya, P. Groche, M.F.-X. Wagner, et al., Particle ejection by jetting and related effects in impact welding processes, Metals 10 (2020) 1108.
- [16] J. Li, B. Schneiderman, S.M. Gilbert, A. Vivek, Z. Yu, G. Daehn, Process characteristics and interfacial microstructure in spot impact welding of titanium to stainless steel, J. Manuf. Process. 50 (2020) 421–429.
- [17] X. Wang, M. Shao, S. Cao, J.-T. Gau, H. Tang, H. Jin, H. Liu, Numerical simulation of laser impact spot welding, J. Manuf. Process. 35 (2018) 396–406.
- [18] G. Daehn, J. Lippold, Low temperature spot impact welding driven without contact, US Patent PCT/US09/36299 11 (2009).
- [19] A.A. Mousavi, S. Al-Hassani, Numerical and experimental studies of the mechanism of the wavy interface formations in explosive/impact welding, Journal of the Mechanics and Physics of Solids 53 (2005) 2501–2528.
- [20] M. Chizari, L. Barrett, Single and double plate impact welding: experimental and numerical simulation, Comput. Mater. Sci. 46 (2009) 828–833.
- [21] M. Chizari, S. Al-Hassani, L. Barrett, Effect of flyer shape on the bonding criteria in impact welding of plates, J. Mater. Process. Technol. 209 (2009) 445–454.
- [22] X. Wang, Y. Zheng, H. Liu, Z. Shen, Y. Hu, W. Li, Y. Gao, C. Guo, Numerical study of the mechanism of explosive/impact welding using smoothed particle hydrodynamics method, Mater. Des. 35 (2012) 210–219.
- [23] X. Wang, Y. Gu, T. Qiu, Y. Ma, D. Zhang, H. Liu, An experimental and numerical study of laser impact spot welding, Mater. Des. 65 (2015) (1980-2015) 1143-1152.
- [24] X. Wang, F. Li, T. Huang, X. Wang, H. Liu, Experimental and numerical study on the laser shock welding of aluminum to stainless steel, Opt. Lasers Eng. 115 (2019) 74–85, https://doi.org/10.1016/j.optlaseng.2018.11.012.
- [25] A. Nassiri, B. Kinsey, Numerical studies on high-velocity impact welding: smoothed particle hydrodynamics(sph) and arbitrary lagrangian–eulerian (ale), J. Manuf. Process. 24 (2016) 376–381.
- [26] R.N. Raoelison, T. Sapanathan, E. Padayodi, N. Buiron, M. Rachik, Interfacial kinematics and governing mechanisms under the influence of high strain rate impact conditions: numerical computations of experimental observations, Journal of the Mechanics and Physics of Solids 96 (2016) 147–161.
- [27] T. Sapanathan, R.N. Raoelison, E. Padayodi, N. Buiron, M. Rachik, Depiction of interfacial characteristic changes during impact welding using computational methods: comparison between arbitrary lagrangian-eulerian and eulerian simulations, Mater. Des. 102 (2016) 303–312.
- [28] A. Nassiri, S. Zhang, T. Lee, T. Abke, A. Vivek, B. Kinsey, G. Daehn, Numerical investigation of cp-ti & cu110 impact welding using smoothed particle hydrodynamics and arbitrary lagrangian-eulerian methods, J. Manuf. Process. 28 (2017) 558–564.
- [29] T. Lee, S. Zhang, A. Vivek, B. Kinsey, G. Daehn, Flyer Thickness Effect in the Impact Welding of Aluminum to Steel, Journal of Manufacturing Science and Engineering 140, 2018.
- [30] Z. Zhang, D. Feng, M. Liu, Investigation of explosive welding through whole process modeling using a density adaptive sph method, J. Manuf. Process. 35 (2018) 169–189.
- [31] V. Gupta, T. Lee, A. Vivek, K.S. Choi, Y. Mao, X. Sun, G. Daehn, A robust processstructure model for predicting the joint interface structure in impact welding, J. Mater. Process. Technol. 264 (2019) 107–118.
- [32] B.C. Liu, A.N. Palazotto, A. Nassiri, A. Vivek, G.S. Daehn, Experimental and numerical investigation of interfacial microstructure in fully age-hardened 15-5 ph stainless steel during impact welding, J. Mater. Sci. 54 (2019) 9824–9842.
- [33] G. Gleason, S. Sunny, S. Sadeh, H. Yu, A. Malik, Eulerian modeling of plasmapressure driven laser impact weld processes, Procedia Manufacturing 48 (2020) 204–214.
- [34] T. Lee, A. Nassiri, T. Dittrich, A. Vivek, G. Daehn, Microstructure development in impact welding of a model system, Scr. Mater. 178 (2020) 203–206.
- [35] J. Cheng, X. Hu, X. Sun, A. Vivek, G. Daehn, D. Cullen, Multi-scale characterization and simulation of impact welding between immiscible mg/steel alloys, Journal of materials science technology 59 (2020) 149–163.
- [36] L.L. Parimi, G. Ravi, D. Clark, M.M. Attallah, Microstructural and texture development in direct laser fabricated in718, Mater. Charact. 89 (2014) 102–111.
- [37] A.A. Antonysamy, J. Meyer, P. Prangnell, Effect of build geometry on the β-grain structure and texture in additive manufacture of ti6al4v by selective electron beam melting, Mater. Charact. 84 (2013) 153–168, https://doi.org/10.1016/j. matchar.2013.07.012.

- [38] S. Sunny, H. Yu, R. Mathews, A. Malik, W. Li, Improved grain structure prediction in metal additive manufacturing using a dynamic kinetic monte carlo framework, Additive Manufacturing (2020) 1–18, https://doi.org/10.1016/j.addma.2020.101649.
- [39] J.C. Heigel, B.M. Lane, Measurement of the Melt Pool Length during Single Scan Tracks in a Commercial Laser Powder Bed Fusion Process, Journal of Manufacturing Science and Engineering 140, 2018.
- [40] A. Handbook, Properties of wrought aluminum and aluminum alloys, ASM International Hand Book Committee 2 (1990) 62–122.
- [41] C. S. Kim, Thermophysical properties of stainless steels, Technical Report, Argonne National Lab., Ill. (USA), 1975.
- [42] C.-H. Hung, A. Sutton, Y. Li, Y. Shen, H.-L. Tsai, M.C. Leu, Enhanced mechanical properties for 304l stainless steel parts fabricated by laser-foil-printing additive manufacturing, J. Manuf. Process. 45 (2019) 438–446.
- [43] A. Foroozmehr, M. Badrossamay, E. Foroozmehr, S. Golabi, Finite element simulation of selective laser melting process considering optical penetration depth of laser in powder bed, Mater. Des. 89 (2016) 255–263.
- [44] B. Zhang, Y. Li, Q. Bai, Defect formation mechanisms in selective laser melting: a review, Chinese Journal of Mechanical Engineering 30 (2017) 515–527.
- [45] P. Michaleris, Modeling metal deposition in heat transfer analyses of additive manufacturing processes, Finite Elem. Anal. Des. 86 (2014) 51–60.
- [46] L.-E. Lindgren, H. Runnemalm, M.O. Näsström, Simulation of multipass welding of a thick plate, Int. J. Numer. Methods Eng. 44 (1999) 1301–1316.
- [47] M. Gouge, P. Michaleris, Thermo-Mechanical Modeling of Additive Manufacturing, Butterworth-Heinemann, 2017.
- [48] J.C. Heigel, P. Michaleris, E.W. Reutzel, Thermo-mechanical model development and validation of directed energy deposition additive manufacturing of ti-6al-4v, Additive manufacturing 5 (2015) 9-19.
- [49] P. Peyre, P. Aubry, R. Fabbro, R. Neveu, A. Longuet, Analytical and numerical modelling of the direct metal deposition laser process, J. Phys. D. Appl. Phys. 41 (2008), 025403.
- [50] V. Neela, A. De, Three-dimensional heat transfer analysis of lens tm process using finite element method, Int. J. Adv. Manuf. Technol. 45 (2009) 935.
- [51] M. Chiumenti, M. Cervera, A. Salmi, C.A. De Saracibar, N. Dialami, K. Matsui, Finite element modeling of multi-pass welding and shaped metal deposition processes, Comput. Methods Appl. Mech. Eng. 199 (2010) 2343–2359.
- [52] V. Manvatkar, A. Gokhale, G.J. Reddy, A. Venkataramana, A. De, Estimation of melt pool dimensions, thermal cycle, and hardness distribution in the laser-engineered net shaping process of austenitic stainless steel, Metall. Mater. Trans. A 42 (2011) 4080–4087
- [53] E.R. Denlinger, J.C. Heigel, P. Michaleris, Residual stress and distortion modeling of electron beam direct manufacturing ti-6al-4v, Proc. Inst. Mech. Eng. B J. Eng. Manuf. 229 (2015) 1803–1813.
- [54] C.-H. Hung, Y. Li, A. Sutton, W.-T. Chen, X. Gong, H. Pan, H.-L. Tsai, M.C. Leu, Aluminum parts fabricated by laser-foil-printing additive manufacturing: processing, microstructure, and mechanical properties, Materials 13 (2020) 414.
- [55] A. Mertens, J. Delahaye, O. Dedry, B. Vertruyen, J.T. Tchuindjang, A.M. Habraken, Microstructure and properties of slm alsi10mg: understanding the influence of the local thermal history, Procedia Manufacturing 47 (2020) 1089–1095.
- [56] C.-D. Wen, Experimental investigation of emissivity of aluminum alloys and application of multispectral radiation thermometry, International Heat Transfer Conference, 49408, 2010, pp. 867–875.
- [57] W. Yan, W. Ge, J. Smith, S. Lin, O.L. Kafka, F. Lin, W.K. Liu, Multi-scale modeling of electron beam melting of functionally graded materials, Acta Mater. 115 (2016) 403–412.
- [58] J. Goldak, A. Chakravarti, M. Bibby, A new finite element model for welding heat sources, Metall. Trans. B 15 (1984) 299–305.
- [59] A. Zinoviev, O. Zinovieva, V. Ploshikhin, V. Romanova, R. Balokhonov, Evolution of grain structure during laser additive manufacturing. Simulation by a cellular automata method, Mater. Des. 106 (2016) 321–329.
- [60] Y. Lian, Z. Gan, C. Yu, D. Kats, W.K. Liu, G.J. Wagner, A cellular automaton finite volume method for microstructure evolution during additive manufacturing, Mater. Des. 169 (2019) 107672.
- [61] Y. Ji, L. Chen, L.-Q. Chen, Understanding microstructure evolution during additive manufacturing of metallic alloys using phase-field modeling, Thermo-Mechanical Modeling of Additive Manufacturing, Elsevier 2018, pp. 93–116.
- [62] X. Wang, K. Chou, Microstructure simulations of inconel 718 during selective laser melting using a phase field model, Int. J. Adv. Manuf. Technol. 100 (2019) 2147–2162
- [63] T.M. Rodgers, J.D. Madison, V. Tikare, Simulation of metal additive manufacturing microstructures using kinetic Monte Carlo, Comput. Mater. Sci. 135 (2017) 78–89.
- [64] K.L. Johnson, T.M. Rodgers, O.D. Underwood, J.D. Madison, K.R. Ford, S.R. Whetten, D.J. Dagel, J.E. Bishop, Simulation and experimental comparison of the thermomechanical history and 3d microstructure evolution of 304l stainless steel tubes manufactured using lens, Comput. Mech. 61 (2018) 559–574.
- [65] T.M. Rodgers, H. Lim, J.A. Brown, Three-dimensional additively manufactured microstructures and their mechanical properties, JOM 72 (2020) 75–82.
- [66] X. Fang, H. Li, M. Wang, C. Li, Y. Guo, Characterization of texture and grain boundary character distributions of selective laser melted inconel 625 alloy, Mater. Charact. 143 (2018) 182–190.
- [67] L.N. Carter, C. Martin, P.J. Withers, M.M. Attallah, The influence of the laser scan strategy on grain structure and cracking behaviour in slm powder-bed fabricated nickel superalloy, J. Alloys Compd. 615 (2014) 338–347.

- [68] Z. Wang, T.A. Palmer, A.M. Beese, Effect of processing parameters on microstructure and tensile properties of austenitic stainless steel 304l made by directed energy deposition additive manufacturing, Acta Mater. 110 (2016) 226–235.
- [69] D. Sun, X. Li, W. Tan, A Parametric Study on Grain Structure in Selective Laser Melting Process for Stainless Steel 316l, in: Proceedings of the 28th Annual International Solid Freeform Fabrication Symposium—An Additive Manufacturing Conference, TX, USA, Austin, 2017 7-9.
- [70] S. Holland, X. Wang, J. Chen, W. Cai, F. Yan, L. Li, Multiscale characterization of microstructures and mechanical properties of inconel 718 fabricated by selective laser melting, J. Alloys Compd. 784 (2019) 182–194.
- [71] S. Plimpton, A. Thompson, A. Slepoy, Stochastic Parallel PARticle Kinetic Simulator, Technical Report, Sandia National Laboratories, 2008.
- [72] C.L. Williams, Structure-property relationships under extreme dynamic environments: shock recovery experiments, Synthesis SEM Lectures on Experimental Mechanics 2 (2019) 1–155.
- [73] C. Williams, K. Ramesh, D. Dandekar, Spall response of 1100-o aluminum, J. Appl. Phys. 111 (2012) 123528.
- [74] X. Wang, H. Zhang, Z. Shen, J. Li, Q. Qian, H. Liu, Experimental and numerical investigation of laser shock synchronous welding and forming of copper/aluminum, Opt. Lasers Eng. 86 (2016) 291–302.
- [75] S.F. Sunny, G.H. Gleason, A.S. Malik, Comparison of numerical methods for fluidstructure interaction simulation of fused deposition modeled nylon components, Procedia Manufacturing 34 (2019) 516–527.
- [76] X. Wang, X. Wang, F. Li, J. Lu, H. Liu, Interface kinematics of laser impact welding of ni and ss304 based on jet indentation mechanism, Metall. Mater. Trans. A (2020) 1–12, https://doi.org/10.1007/s11661-020-05733-0.
- [77] N. Rusin, A. Skorentsev, E. Kolubaev, Dry friction of pure aluminum against steel, Journal of Friction and Wear 37 (2016) 86–93.
- [78] K. Ding, L. Ye, Laser Shock Peening: Performance and Process Simulation, Woodhead Publishing, 2006.
- [79] M.I. Hatamleh, J. Mahadevan, A. Malik, D. Qian, R. Kovacevic, Prediction of Residual Stress Random Fields for Selective Laser Melted a357 Aluminum Alloy Subjected to Laser Shock Peening, Journal of Manufacturing Science and Engineering 141, 2019.
- [80] X. Hong, S. Wang, D. Guo, H. Wu, J. Wang, Y. Dai, X. Xia, Y. Xie, Confining medium and absorptive overlay: their effects on a laser-induced shock wave, Opt. Lasers Eng. 29 (1998) 447–455.
- [81] B. Mohammed, T. Park, F. Pourboghrat, J. Hu, R. Esmaeilpour, F. Abu-Farha, Multiscale crystal plasticity modeling of multiphase advanced high strength steel, Int. J. Solids Struct. 151 (2018) 57–75.
- [82] E. Hall, The deformation and ageing of mild steel: iii discussion of results, Proceedings of the Physical Society. Section B 64 (1951) 747.
- [83] N. Petch, The fracture of metals, Prog. Met. Phys. 5 (1954) 1–52.
- [84] R.W. Armstrong, Engineering science aspects of the hall-petch relation, Acta Mech. 225 (2014) 1013–1028.
- [85] L.-E. Lindgren, A. Lundbäck, M. Fisk, R. Pederson, J. Andersson, Simulation of additive manufacturing using coupled constitutive and microstructure models, Additive Manufacturing 12 (2016) 144–158.
- [86] A.D. Schino, I. Salvatori, J. Kenny, Effects of martensite formation and austenite reversion on grain refining of aisi 304 stainless steel, J. Mater. Sci. 37 (2002) 4561–4565.
- [87] N. Kamikawa, X. Huang, N. Tsuji, N. Hansen, Strengthening mechanisms in nanostructured high-purity aluminium deformed to high strain and annealed, Acta Mater. 57 (2009) 4198–4208.
- [88] J. Robinson, The mechanics of wave formation in impact welding, The Philosophical Magazine: A Journal of Theoretical Experimental and Applied Physics 31 (1975) 587–597.
- [89] R. Menikoff, Empirical equations of state for solids, Shock-Wave Science and Technology Reference Library, Springer 2007, pp. 143–188.
- [90] W. Harrison, C. Loupias, P. Outrebon, D. Turland, Experimental data and hydrocode calculations for hypervelocity impacts of stainless steel into aluminium in the 2–8 km/s range, International journal of impact engineering 17 (1995) 363–374.
- [91] W. Isbell, F. Shipman, A. Jones, Hugoniot Equation of State Measurements for Eleven Materials to Five Megabars, Technical Report, GENERAL MOTORS TECHNICAL CENTER WARREN MI MATERIALS AND STRUCTURES LAB, 1968.
- [92] B. Dodd, Y. Bai, Adiabatic Shear Localization: Frontiers and Advances, Elsevier, 2012.
- [93] L.E. Murr, E. Trillo, S. Pappu, C. Kennedy, Adiabatic shear bands and examples of their role in severe plastic deformation, J. Mater. Sci. 37 (2002) 3337–3360.
- [94] Z. Zhang, D.E. Eakins, F.P. Dunne, On the formation of adiabatic shear bands in textured hcp polycrystals, Int. J. Plast. 79 (2016) 196–216.
   [95] S. Boakve-Yiadom. N. Bassim. Microstructural evolution of adiabatic shear bands in
- pure copper during impact at high strain rates, Mater. Sci. Eng. A 711 (2018) 182–194.
- [96] L. Tang, Z. Chen, C. Zhan, X. Yang, C. Liu, H. Cai, Microstructural evolution in adiabatic shear bands of copper at high strain rates: Electron backscatter diffraction characterization, Mater. Charact. 64 (2012) 21–26.
- [97] K.K. Alaneme, E.A. Okotete, Recrystallization mechanisms and microstructure development in emerging metallic materials: a review, Journal of Science: Advanced Materials and Devices 4 (2019) 19–33.
- [98] S.V. Astafurov, G.G. Maier, E.V. Melnikov, V.A. Moskvina, M.Y. Panchenko, E.G. Astafurova, The strain-rate dependence of the hall-petch effect in two austenitic stainless steels with different stacking fault energies, Mater. Sci. Eng. A 756 (2019) 365–372.
- [99] I. Karaman, H. Sehitoglu, Y. Chumlyakov, H. Maier, The deformation of lowstacking-fault-energy austenitic steels, Jom 54 (2002) 31–37.

- [100] F.J. Humphreys, M. Hatherly, Recrystallization and Related Annealing Phenomena, Elsevier, 2012.
- [101] Z. Zhu, W. Li, Q.B. Nguyen, X. An, W. Lu, Z. Li, F.L. Ng, S.M.L. Nai, J. Wei, Enhanced strength-ductility synergy and transformation-induced plasticity of the selective laser melting fabricated 304 l stainless steel, Additive Manufacturing 101300
- [102] B. Hutchinson, Deformation microstructures and textures in steels, philosophical transactions of the Royal Society of London, Series A: Mathematical, Physical and Engineering Sciences 357 (1999) 1471–1485.
- [103] D. Raabe, Recovery and recrystallization: phenomena, physics, models, simulation, Physical Metallurgy, Elsevier 2014, pp. 2291–2397.
- [104] R. Stevens, Grain-boundary sliding in metals, Metallurgical Reviews 11 (1966) 129-142.
- [105] Y. Zhang, S.S. Babu, C. Prothe, M. Blakely, J. Kwasegroch, M. LaHa, G.S. Daehn, Application of high velocity impact welding at varied different length scales, J. Mater. Process. Technol. 211 (2011) 944–952.

  [106] S.A. Mousavi, S. Al-Hassani, Finite element simulation of explosively-driven plate
- impact with application to explosive welding, Mater. Des. 29 (2008) 1–19.
- [107] J.G. Kaufman, PFire Resistance of Aluminum and Aluminum Alloys: & Measureing the Effects of Fire Exposure on the Properties of Aluminum Alloys (2016) 1–6.

  [108] X. He, J. Norris, P. Fuerschbach, T. DebRoy, Liquid metal expulsion during laser spot
- [108] A. Re, J. Norris, F. refescibacti, T. Debroy, Edular finetal expulsion during faser spot welding of 304 stainless steel, J. Phys. D. Appl. Phys. 39 (2006) 525.
  [109] J. Robinson, Fluid mechanics of copper: viscous energy dissipation in impact welding, J. Appl. Phys. 48 (1977) 2202–2207.
  [110] J.G. Kaufman, Fire Resistance of Aluminum and Aluminum Alloys, ASM Interna-
- tional, Materials Park, Ohio, 2016.